AGU PUBLICATIONS

JGR

Journal of Geophysical Research: Atmospheres

RESEARCH ARTICLE
10.1002/2015JD023123

Key Points:
- First multiaircraft observations of SHL core region
- Two moisture transport pathways identified in observations
- Afternoon CBL overestimation causes moisture transport error in Africa-LAM

Correspondence to:
S. Engelstaedter,
sebastian.engelstaedter@ouce.ox.ac.uk

Citation:
Engelstaedter, S., R. Washington, C. Flamant, D. J. Parker, C. J. T. Allen, and M. C. Todd (2015), The Saharan heat low and moisture transport pathways in the central Sahara—Multiaircraft observations and Africa-LAM evaluation, *J. Geophys. Res. Atmos.*, *120*, 4417–4442, doi:10.1002/2015JD023123.

Received 16 JAN 2015
Accepted 3 APR 2015
Accepted article online 8 APR 2015
Published online 18 MAY 2015

The Saharan heat low and moisture transport pathways in the central Sahara—Multiaircraft observations and Africa-LAM evaluation

S. Engelstaedter[1], R. Washington[1], C. Flamant[2], D. J. Parker[3], C. J. T. Allen[1], and M. C. Todd[4]

[1]Climate Research Lab, Oxford University Centre for the Environment, Oxford, UK, [2]Laboratoire Atmosphères, Milieux, Observations Spatiales, CNRS, Sorbonne Universités, UPMC and UVSQ, Paris, France, [3]School of Earth and Environment, University of Leeds, Leeds, UK, [4]Department of Geography, University of Sussex, Brighton, UK

Abstract We present a characterization of the Saharan heat low (SHL) based on dropsonde observations made on 22 June 2011 by two simultaneously flying aircraft during the Fennec project. The observations are used to identify moisture transport pathways and to validate the UK Met Office limited area model for northern Africa (Africa-LAM). The observations capture the SHL, harmattan, and monsoon surge. The SHL has a northeast-southwest orientated elongated shape centered over northern Mauritania. The SHL core is associated with a 950 hPa temperature minimum (36.4°C) in the morning caused by the monsoon surge and a maximum (42.6°C) in the afternoon. The monsoon surge east of the SHL core splits into two transport pathways: (a) curving around the SHL core in the north, especially pronounced in a morning near-surface layer, and (b) northeastward transport within the ~2 km deep monsoon surge (afternoon observations only). In the morning the model forecasts the harmattan, monsoon surge, and the SHL geographic location and northeast-southwest orientation well but the model represents the SHL flatter and more spatially extended and overestimates the convective boundary layer (CBL) by up to ~0.3 km. The simulated afternoon SHL location appears shifted westward by up to ~1°. The model overestimates the shallow afternoon monsoon surge CBL depth of ~1.8 km by >2 km resulting in southwestward transport of vertically mixed moisture above ~2.5 km contrasting observed northeastward-only transport at lower levels. This moisture distribution model error is likely to have consequences for simulations of Saharan thermodynamics and dust emissions caused by convection-driven cold pools.

1. Introduction

The Sahara desert is dominated by extreme environmental conditions. Large-scale subsidence of air results in a hyperarid almost vegetation-free uninhabited environment. In the northern hemisphere summer, surface heating from intense solar radiation leads to the development of a near-surface thermal low pressure system over northern Mali, southern Algeria, and eastern Mauritania, commonly referred to as the Saharan heat low (SHL) [*Lavaysse et al.*, 2009; *Messager et al.*, 2010]. The SHL has been identified as an important climatic system that interacts with the midlatitudes [*Knippertz*, 2007; *Chauvin et al.*, 2010; *Lavaysse et al.*, 2010a; *Roehrig et al.*, 2011], the West African monsoon system [*Sultan and Janicot*, 2003; *Parker et al.*, 2005; *Peyrille et al.*, 2007], and the northern tropical Atlantic, [*Grams et al.*, 2010; *Evan et al.*, 2011] highlighting its role as a significant climatic driver on regional to continental scales [*Lafore et al.*, 2011]. Specifically, the seasonal and intraseasonal variabilities of the SHL seem to be linked to the onset, temporal evolution, and strength of the West African Monsoon, which affects the livelihood of millions of people in the Sahel [*Sultan and Janicot*, 2003; *Lavaysse et al.*, 2010b; *Roehrig et al.*, 2011]. Synoptic-scale oscillations in SHL intensity can alter the intraseasonal variability of Sahelian precipitation; during a strong (warm) phase of the SHL, there is an intensification of the SHL low-level cyclonic circulation, favoring increased deep convection in the central and eastern Sahel because of the anomalous surface southerlies and convection suppression in the western Sahel due to the anomalous surface northerlies [*Lavaysse et al.*, 2010b]. Recently, *Evan et al.*, 2015 have shown that the rise in temperature in the SHL region observed in the last 30 years is due to greenhouse warming by water vapor and that the structure of the drought recovery over Sahel is consistent with a warming SHL and is evidence of a fundamental, but not exclusive, role for the SHL in the recent increase in Sahelian monsoon rainfall. Working on model projections from the Coupled Model Intercomparison Project 3 (CMIP3), *Biasutti et al.* [2009] have shown that the trend in future

Sahel rainfall is closely related to the intensity of the SHL, although the coupling of these systems mean that cause and effect are not clear in this result.

The heating pattern in the SHL has a domed shape reaching up to about 700 hPa [*Thorncroft and Blackburn*, 1999]. The resulting upward motion of air is associated with a lower troposphere cyclonic circulation around the SHL that enhances the monsoon and harmattan flow south and north of the heating maximum, respectively. An anticyclonic circulation prevails at about 700 hPa and above that leads to an acceleration of the African Easterly Jet [*Thorncroft and Blackburn*, 1999]. Large-scale descending air in the tropics as part of the poleward branch of the Hadley cells leads to high-pressure belt at about 500 hPa contrasting the SHL in the lower troposphere. Low-level atmospheric thickness (LLAT) (difference between 700 and 950 hPa geopotential height) has been shown to be a good metric for locating the SHL [*Lavaysse et al*., 2009]. It correlates well with 850 hPa air temperature [*Lavaysse et al*., 2013].

The Sahara is the world's largest and most active dust source region [*Prospero et al*., 2002; *Washington et al*., 2003], and dust is semipermanent in the overlying atmosphere during Northern Hemisphere summer [*Israelevich et al*., 2003] with dry convection mixing the dust within one of the deepest atmospheric boundary layers on the planet (up to 6 km) [*Gamo*, 1996; *Cuesta et al*., 2008; *Garcia-Carreras et al*., 2014]. Satellite-derived observations of dust aerosol distributions and reanalysis data sets show that the SHL develops contemporaneously with increasing dust concentrations to reach a simultaneous peak in June [*Engelstaedter et al*., 2006]. The specific reasons for the spatiotemporal co-location of the SHL and peak atmospheric dust loadings remain poorly understood. *Allen et al*. [2013] show that 45% of atmospheric dust observed at Bordj Badji Mokhtar in southern Algeria (close to the SHL core region) is generated by cold pool outflow emission in the region and cold pool advection accounts for an additional 27% of dust. *Bou Karam et al*. [2014] present a detailed analysis of a synoptic-scale 3 day dust event in August 2006 caused by a mesoscale convective system cold pool estimating an average total dust load of 1.5 Tg. These results indicate that SHL-associated moisture transport into the hyperarid central Sahara plays a critical role fuelling this major dust emission mechanism which could in part explain the co-location of the SHL and highest dust loadings in Boreal summer.

While the meridional shift of the intertropical convergence zone controls the seasonal cycle of precipitation in the Sahel, intraseasonal moisture variability in spring and summer is modulated by equatorial Rossby waves, Kelvin waves, and tropical disturbances [e.g., *Mera et al*., 2014, and references therein]. They also contribute to the initiation and intensification of the synoptic disturbances over the Sahel that can enhance poleward low-level moisture transport into the Sahara. These disturbances affect the moisture and temperature budget in the region and yield meteorological conditions that are detrimental to the maintenance of a strong SHL at synoptic time scales. Midlatitude Rossby waves are also known to affect the position of the SHL over the Sahara through wave breaking processes [*Chauvin et al*., 2010]. A weakening of the SHL is thought to lead to a weaker African Easterly Jet [*Thorncroft and Backburn*, 1999], but, in general, the potential impact of the SHL on transient equatorial features is little studied. This is in part the result of only very limited observations being available from the SHL region. The distribution of weather stations in western Africa (not all report regularly) exposes a lack of routine observations in a region roughly the size of western Europe (Figure 1). Therefore, our understanding of the SHL, atmospheric dust distribution, and moisture distribution in the central Sahara is based solely on remotely sensed products, numerical models, and radiosonde observations from isolated locations at the fringes of the SHL region (e.g., Tamanrasset and In Salah, Algeria; Figure 1). Given the importance of the SHL and the associated maximum in aerosol loadings, there is a critical need for observational studies to verify the products on which the science has come to depend. The focus of previous field campaigns in the broad region, such as the African Monsoon Multidisciplinary Analyses (AMMA) program [*Lebel et al*., 2010], the Dust And Biomass Experiment [*Johnson et al*., 2009], the Saharan Mineral Dust Experiment [*Ansmann et al*., 2011], the Dust Outflow and Deposition to the Ocean experiment [*McConnell et al*., 2010], and the Geostationary Earth Radiation Budget Intercomparison of Longwave and Shortwave radiation [*Haywood et al*., 2011], was not the central Sahara where the SHL develops. *Messager et al*. [2010] describe the first airborne measurements over the central Sahara made opportunistically on AMMA transit flights: these results are compelling, in showing remarkable structure in the boundary layer of the SHL, but did not sample consistently in time or space and were not able to observe the heart of the SHL itself. These limited observations are not sufficient to address the spatial variability and temporal evolution of the SHL in the central western Sahara and do not allow for the evaluation of

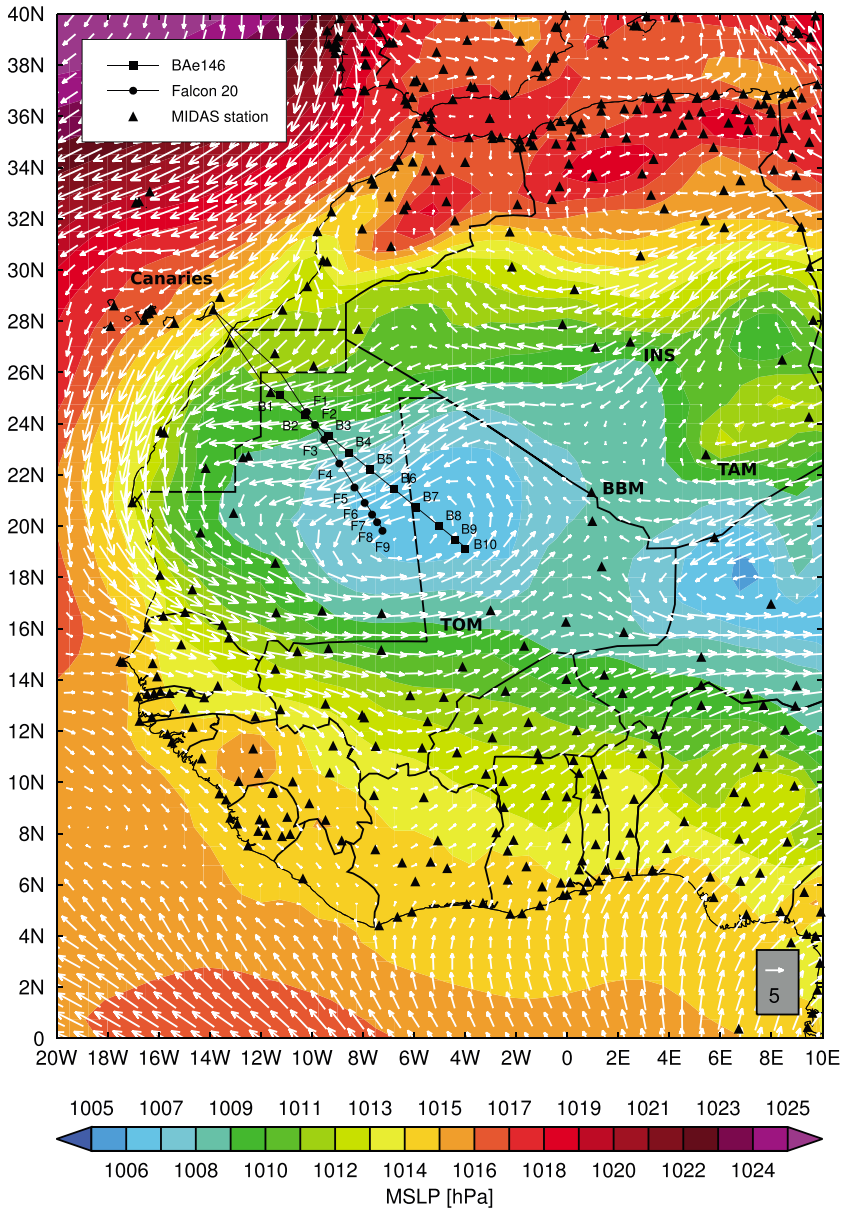

Figure 1. ERA-Interim mean sea level pressure (color contour) and 950 hPa wind vectors (white arrows) over western Africa on 22 June 2011 at 12 UTC. The reference arrow shown at the left bottom corner is 5 m s^{-1}. Overlain are the flight tracks and dropsonde locations labeled B1 to B10 for the BAe146 and F1 to F9 for the F-20, respectively. The distribution of weather stations derived from the UK Meteorological Office Integrated Data Archive System (MIDAS) Global Weather Observation archive (GL) (http://badc.nerc.ac.uk/data/ukmo-midas/GL_Table.html) is shown by brown triangles. Reference labels were added for In Salah (INS), Tamanrasset (TAM), Bordj Badji Mokhtar (BBM), Tombouctou (TOM), and the Canary Islands.

simulations of SHL characteristics, dust distributions, and moisture transport in climate and numerical weather prediction (NWP) models.

The "Fennec—The Saharan Climate System" project [*Washington et al.*, 2012] aimed at deriving a definitive climate data set for the central Sahara from ground, aircraft, and satellite observations to characterize thermodynamic, dynamic, and compositional structure of the central Sahara's atmosphere and to challenge weather prediction and climate models. Results from Fennec's ground observations [*Marsham et al.*, 2013; *Todd et al.*, 2013; *Garcia-Carreras et al.*, 2014] have begun to explain the dynamic and thermodynamic structure of the Saharan boundary layer, which is dominated by a strong diurnal cycle of

mixing and advection and shows significant sensitivity to moisture advection. However, the ground observations are by necessity limited in spatial resolution. As part of the Fennec project extended aircraft detachment, two research aircraft operating out of Fuerteventura (Canary Islands, Spain) surveyed the troposphere in the SHL region on 22 June 2011 (Figure 1). The SHL was forecast to be centered close to the Mauritania-Mali border on that day. The two aircraft flew simultaneously in the morning and in the afternoon into the SHL core region on two different tracks, thereby sampling the atmosphere with dropsondes, active, and passive remote sensing instruments (LIDARs and radiometers, respectively) and in situ sampling instrumentation along each track four times (Figure 1), in the morning and in the afternoon. These unique aircraft measurements, complemented by ground instrumentation and satellite observations, allow for a comprehensive survey of the SHL and the processes and dynamics that operate in the SHL core region. Although the aircraft observations represent only a single-day snapshot of the SHL in time, they are nevertheless the first nonremotely sensed spatial observations from the core region of the SHL. Given the importance of the SHL in the climate system, we argue that the analysis of the considerable data set from these flights is an important first step in building the observational data necessary to evaluate numerical model products for this key region. The multiple flights into the SHL on that day allow for an analysis of how the SHL properties and associated moisture transport changed between the morning and afternoon and for testing how well a regional forecast model is able to simulate the SHL spatial structure.

In this paper we focus (a) on the analysis and characterization of the SHL and associated moisture transport pathways in the morning and afternoon of 22 June 2011 based on dropsonde observations from the two research aircraft and (b) on testing how well the UK Meteorological Office Limited Area Model configuration for North Africa (Africa-LAM) is able to forecast the SHL location, intensity, and structure as well as the associated moisture transport pathways which are critical for the development of convection and cold pool associated dust emissions. The development of the convective boundary layer (CBL) and atmospheric dust detected during these flights (satellite imagery shows no dust that day) will be addressed in an additional paper. We first describe the measurements, data, and methodology used in the study (section 2) followed by a brief analysis of the large-scale meteorological conditions leading up to the 22 June 2011 (section 3). We then present the observation-based analysis of the SHL and associated moisture transport (section 4) and the evaluation of the Africa-LAM (section 5) followed by discussion (section 6) and summary and conclusions (section 7).

2. Data and Processing

2.1. Dropsonde Measurements

On 22 June 2011, two research aircraft flew simultaneously from Fuerteventura (Canary Islands, Spain) on different transects across Mauritania and northern Mali in order to measure changes in the atmospheric conditions in the SHL core region associated with the daytime evolution of the Saharan troposphere (Figure 1). Flights were made in the morning and afternoon. The UK research aircraft, a modified BAe-146-301 (hereafter BAe146), is owned by BAE systems and operated by DirectFlight (http://www.directflight.co.uk) in conjunction with the Facility for Airborne Atmospheric Measurements (FAAM). Between 8:44 and 11:57 UTC, the BAe146 flew a transect from the Western Sahara/Mauritania border at 25.7°N/12°W to 19.8°N/4.8°W (flight B607, Figure 1). During the afternoon flight B608 between 15:49 to 19:33 UTC, the transect was extended to the east to 19.1°N/3.9°W over Mali in order to fully capture the center of the SHL. The BAe146 flew at an altitude of 25 kft (7.62 km) above mean sea level (MSL) during the transects of flight B607 and outward leg of flight B608. During the return leg of flight B608, the aircraft flew at 28 kft (8.53 km) above MSL.

The French research aircraft is a modified Dassault Falcon 20 GF (hereafter F-20) operated by the Service des Avions Français Instrumentés pour la Recherche en Environnement (SAFIRE, a joint entity of Centre National de la Recherche Scientifique (CNRS), Météo-France, and Centre National d'Etudes Spatiales (CNES)). Corresponding to the BAe146 flights B607 and B608, the F-20 made two flights, one in the morning (flight F24) between 11:01 UTC and 12:09 UTC and one in the afternoon (flight F25) between 17:00 UTC and 18:11 UTC, along transects from the Western Sahara/Mauritania border at 26.02°N/11.25°W to 19.87°N/7.22°W

Table 1. Dropsonde Release Times[a]

Bae146 Sonde Location	B607 Out	B607 Return	B608 Out	B608 Return
B1	08:53	11:46	15:58	19:24
B2	09:05	11:34	16:11	19:10
B3	09:18	11:22	16:24	18:55
B4	09:28	11:10	—	—
B5	09:39	10:58	16:45	18:34
B6	09:50	10:45	16:57	18:19
B7	10:01	10:32	17:09	18:06
B8	10:19	—	17:21	17:53
B9	—	—	17:29	—
B10	—	—	17:38	—
Faclon 20 Sonde Location	F24 Out	F24 Return	F25 Out	F25 Return
F1	10:11	—	—	—
F2	—	—	16:21	17:50
F3	10:21	11:42	16:27	—
F4	10:30	11:31	16:34	17:35
F5	10:40	11:20	16:42	—
F6	—	—	16:50	17:18
F7	10:50	11:10	—	—
F8	—	—	16:57	—
F9	10:56	—	17:00	—

[a]Time given in UTC for each dropsonde released during BAe146 flights B607 and B608 as well as Falcon 20 flights F25 and F26 on 22 June 2011. See Figure 1 for dropsonde locations and flight tracks.

at an altitude of 11 km above MSL (Figure 1). Since the F-20 flies faster than the BAe146, the flights were timed to coincide with near-simultaneous turning points at the eastern edge of the transects.

Dropsondes were released over Mauritania and Mali on 22 June 2011 at predefined coordinates along both flight tracks (Figure 1) using identical onboard Vaisala Airborne Vertical Atmospheric Profiling System GPS systems for RD94 dropsondes. A total of 15, 10, 16, and 10 dropsondes were released during flights B607, F24, B608, and F25, respectively. Note that the time difference between dropsonde releases at the sonde locations during the outward and return legs decreases from west to east ranging between 173 (B1) and 31 (B7) min in the morning and between 206 (B1) and 28 (F6) min in the afternoon (see Table 1 for release times). Between the morning return and afternoon outgoing flights, the time difference between repeat sampling ranges between 4 h 12 min (B1) and more than 7 h (B8). Quality control processing of the dropsonde data was performed using the Atmospheric Sounding Processing Environment (ASPEN) software v3.1-7562 provided by NCAR (http://www.eol.ucar.edu/data/software/aspen).

The dropsondes measure pressure, temperature, and relative humidity every 0.5 s. The instrumental measurement errors are expressed as accuracy repeatability which is the standard deviation of differences between two successive repeated calibrations ($k = 2$ confidence level) and were obtained from the RD94 technical data sheet (http://cn.vaisala.com/Vaisala%20Documents/Brochures%20and%20Datasheets/RD94-Dropsonde-Datasheet-B210936EN-A-LoRes.pdf). Pressure, temperature, and relative humidity measurements have a resolution (accuracy repeatability) of 0.1 hPa (0.4 hPa), 0.1°C (0.2°C), and 1% (2%), respectively. Wind speed is measured up to every 0.25 s, and errors are in the range of $\pm 0.5\ m\ s^{-1}$. Based on these errors, Monte Carlo simulations were performed with 1000 runs for each BAe146 dropsonde yielding a mean standard error for water vapor mixing ratio (WVMR) of about $0.6\ g\ kg^{-1}$ at 0.5 km above MSL (close to the surface) gradually decreasing with height to about 0.3 and 0.1 g/kg at 2 and 4 km, respectively. The standard error for the horizontal moisture flux is about 5.3, 3.0, and $1.5\ g\ m\ kg^{-1}\ s^{-1}$ at 0.5, 2.0, and 4.0 km above MSL, respectively. Dropsondes have a descent speed of about $11\ m\ s^{-1}$ near the surface which means that the last measured pressure level over water is at maximum about 5.5 m above the water surface. Over land, more accurate surface pressure measurements can be achieved because the sondes continue to broadcast after they reach the surface. Therefore, the raw data of each dropsonde were manually inspected to identify the correct surface pressure and the time when the dropsonde reached the surface. The last measurement time was then used to override the ASPEN reported end-of-drop time in cases where it differed. Upward integration from the surface was performed by the ASPEN software whereby the surface altitude was

derived from the Advanced Spaceborne Thermal Emission and Reflection Radiometer (ASTER) Global Digital Elevation Model (DEM) v2 available at 30 m horizontal resolution [*Tachikawa et al*., 2011] at the geographic location where the dropsonde reached the ground. Over the conterminous United States, an overall absolute vertical accuracy at the 95% confidence level of 17.01 m and a root-mean-square error of 8.68 m was reported by *Gesch et al*. [2011] for ASTER DEM v2 with respect to GPS benchmarks whereby land cover types classified as "Open" showing a slight negative bias of −0.95 m in the mean error. For the purpose of reproducibility, we here include the dropsonde and processing details for each sonde in Table 2.

2.2. Africa-LAM and ERA-Interim

As part of the Fennec field campaign operations, the UK Meteorological Office provided daily forecasts using its Africa Limited Area Model (Africa-LAM), a special configuration of the UK Meteorological Office Unified Model [*Cullen*, 1993]. The Africa-LAM is a nonhydrostatic, finite difference model run over the north African domain (19.89°W–52.93°E, 0.04°N–44.81°N). The Africa-LAM employs 3D-Var assimilation and was initialized each day at 18 UTC using boundary conditions provided by the 12 UTC initialized run of the UK Meteorological Office global forecast model [*Walters et al*., 2011], which runs at 0.5625 by 0.375° horizontal resolution, 50 model levels, and a forecast length of 144 h. Each forecast of the Africa-LAM is over 58 h. The variables pressure, air temperature, and relative humidity are available in 1-hourly time steps whereas wind speed and direction are available at 3-hourly time steps. The Africa-LAM output is available at 0.11° by 0.11° horizontal resolution and 70 vertical levels. Sondes that were dropped on 22 June 2011 as part of flights B607 and B608 analyzed in this paper were assimilated into the ERA-Interim reanalysis which drives the Africa-LAM forecasts. However, Africa-LAM forecasts to be analyzed here correspond to the 18 UTC initialized forecast from 21 June 2011 and are therefore independent of the data from the dropsondes. While the primary driver of the heat low pressure configuration is surface heating, the observations are also affected by diurnal and semidiurnal tides in surface pressure that over the study region have a June-July-August amplitude of about 0.7 to 0.8 hPa and 0.8 to 0.9 hPa, respectively [*Dai and Wang*, 1999]. However, station scarcity in the central Sahara will increase the uncertainty of these estimates which are based on station and marine pressure data. The Africa-LAM was chosen as a regional modeling tool because (a) measurements from remote automatic weather stations deployed in Mauritania and Algeria as part of the Fennec campaign were assimilated [*Hobby et al*., 2012], (b) it runs at a high spatial resolution over the western Africa domain, (c) it simulates the Harmattan low-level jet (LLJ) at Bordj Badji Mokhtar in southern Algeria remarkably well in comparison to ERA-Interim [*Allen and Washington*, 2014], and (d) it was a major objective of the Fennec project to improve UK Meteorological Office numerical forecasting tools for northern Africa.

The dropsonde observations vary significantly in space and time (e.g., 3 h and 26 min between first and last dropsondes of BAe146 afternoon flight; see Table 1) which does not allow for a simple comparison of the observations with the spatial pattern of a variable at a specific model forecast time step. Therefore, the following approach was chosen for the comparison of the dropsonde observations with the Africa-LAM in section 5. First, the model output was interpolated in the horizontal domain to the geographic location of each sonde using bilinear interpolation. Second, linear interpolation was used to interpolate the model data in the vertical domain to the 950, 700, and 500 hPa pressure levels. The chosen main pressure level for the analysis in this paper was 950 hPa because it captures the near-surface cyclonic circulation at the bottom of the SHL which is important for moisture transport from the monsoon. The 700 hPa pressure level captures the anticyclonic circulation at the top of the SHL and is used in the calculation of low-level atmospheric thickness (see section 2.3). ERA-Interim 500 hPa geopotential height is used only in the discussion of large-scale atmospheric features in section 3. In a third step, the Africa-LAM data were interpolated in the time domain to the release time of each sonde using linear interpolation. The time interpolation is likely to be associated with the largest uncertainties. All model fields are available in 1-hourly time steps with the exception of wind fields which are available in 3-hourly time steps. The error associated with the time interpolation is likely to be largest in the morning hours when variables such as temperature, pressure, and wind speed change rapidly after sunrise and the CBL starts to develop. In addition, observations may not change linearly between two model time steps. Nevertheless, the approach chosen allows for the closest comparison of the observations and model data in space and time.

Table 2. Dropsonde Details[a]

Sonde Location	Longitude [°]	Latitude [°]	ASTER-Derived Surface Altitude [m]	End-of-Drop Time in Raw Data [s]	ASPEN QC Surface Pressure [hPa]
B1	−11.166375	25.150803	316	651.26	977.2
B2	−10.280441	24.382828	269	461.25	981.5
B3	−9.309093	23.490141	231	583.23	984.2
B4	−8.544725	22.862909	305	623.75	977.3
B5	−7.684660	22.156855	329	620.75	973.4
B6	−6.778950	21.438229	324	629.50	971.7
B7	−5.910832	20.714592	278	628.25	976.6
B8	−5.020446	19.994961	289	642.51	974.6
B7	−5.915713	20.729004	284	605.68	976.2
B6	−6.775296	21.444864	319	598.26	972.9
B5	−7.675697	22.174026	318	453.75	975.1
B4	−8.546223	22.865185	302	620.00	976.2
B3	−9.419380	23.594641	256	466.26	983.5
B2	−10.285429	24.310406	270	619.25	983.4
B1	−11.162410	25.031313	299	606.26	977.0
B1	−11.324973	25.145620	330	700.26	972.6
B2	−10.275652	24.372456	243	557.26	979.9
B3	−9.297917	23.483503	244	580.75	980.9
B5	−7.677357	22.154850	329	648.76	971.7
B6	−6.771774	21.453615	309	492.75	969.7
B7	−5.910484	20.725101	273	625.25	973.2
B8	−5.013978	19.988098	286	480.75	973.5
B9	−4.409281	19.458025	297	630.00	973.7
B10	−4.018499	19.113605	276	625.76	975.1
B8	−5.016599	19.982527	297	604.50	972.8
B7	−5.910791	20.711973	282	717.51	974.2
B6	−6.772197	21.450554	316	511.01	971.7
B5	−7.812657	22.288197	335	486.90	969.6
B3	−9.300928	23.477209	235	723.26	980.4
B2	−10.273622	24.363098	253	700.75	980.5
B1	−11.314954	25.141861	324	661.26	971.8
F1	−10.203910	24.455999	258	831.29	980.4
F3	−9.557000	23.446260	225	810.23	984.0
F4	−8.924200	22.432911	275	800.79	978.1
F5	−8.281180	21.430321	358	821.79	968.5
F7	−7.639860	20.439569	348	843.74	969.3
F9	−7.229640	19.811510	331	775.40	970.5
F7	−7.679320	20.507650	348	773.50	967.3
F5	−8.296260	21.447920	364	817.45	968.1
F4	−8.935420	22.450291	260	824.70	980.6
F3	−9.573960	23.473009	225	674.70	984.2
F2	−9.840490	23.890940	242	768.01	981.6
F3	−9.417760	23.203409	225	880.64	982.0
F4	−8.927940	22.434931	278	786.28	972.9
F5	−8.388030	21.586260	367	798.51	963.2
F6	−7.904870	20.858271	365	772.50	965.2
F8	−7.446650	20.151581	330	776.84	967.4
F9	−7.238540	19.820721	337	802.34	967.6
F6	−7.935290	20.907669	360	789.39	963.9
F4	−8.926970	22.459120	264	649.74	976.6
F2	−9.879080	23.957291	239	844.19	981.0

[a]Latitude and longitude coordinates indicate where the sonde hits the surface. For the purpose of reproducibility, the raw data end-of-drop time and ASPEN software-calculated quality control-checked surface pressure are also given.

European Centre for Medium-Range Weather Forecasts (ECMWF) interim reanalysis (ERA-Interim) [*Dee et al.*, 2011] fields are used to put the large-scale 22 June 2011 atmospheric conditions into the climatological perspective because no long-term runs are available from the Africa-LAM. Full resolution ERA-Interim mean sea level pressure (MSLP) and 10 m zonal and meridional wind component fields (U and V, respectively) available at 0.7° by 0.7° spatial resolution were obtained from the ECMWF website (http://www.ecmwf.int).

2.3. Calculations of GPH, LLAT, CBL Depth, and Horizontal Moisture Flux

Geopotential height (GPH) at 950 hPa (GPH_{950}) and 700 hPa (GPH_{700}) was calculated for each dropsonde by first interpolating the altitudes associated with the pressure measurements to the pressure level and then calculating GPH using

$$\mathrm{GPH} = g / g_0 * Z, \tag{1}$$

where g is the gravitational acceleration at a given latitude and height, g_0 is the average gravitational acceleration at MSL ($g_0 = 9.80665\ \mathrm{ms}^{-2}$), and Z is the altitude above MSL of the 950 hPa pressure level. Approximations for g were derived from

$$g = 9.780327\left(1 + A\ \sin^2(L) - B\ \sin^2(2L)\right) - 3.086\times10^{-6}H, \tag{2}$$

whereby A is 0.0053024, B is 0.0000058, L is the latitude of the dropsonde location where the sonde reached the surface, and H is the altitude above MSL of the pressure level. Low-level atmospheric thickness (LLAT) [*Lavaysse et al*., 2009] was then calculated as the difference between GPH_{700} and GPH_{950}. It has errors of approximately ±1 m.

The boundary layer depth was determined by locating the altitude in the sonde record where the potential air temperature (T_{pot}) first reaches 0.3°C above the value at 150 m above the surface. In cases where T_{pot} increased monotonically from the surface up to 150 m, the surface T_{pot} value was used as a reference. *Marsham et al*. [2013] and *Todd et al*. [2013] defined the top of the boundary layer in Fennec supersite 1 and 2 radiosonde observations as the height where the virtual potential air temperature first reaches 0.5°C above the value at 930 hPa and water vapor mixing ratio first falls to 0.5 $\mathrm{g\,kg}^{-1}$ below the value at 930 hPa. Here, we used a slightly different approach because (a) the fixed pressure level of 930 hPa is at times close to the very shallow boundary layer in the morning observations, (b) the surface elevation varies between the dropsonde locations, and (c) moisture transport into the region by the monsoon surge can lead to increased moisture levels above the boundary layer in the morning when the CBL starts to develop.

Horizontal moisture flux (HMF) was calculated by multiplying the WVMR with the wind vectors. The vertically integrated HMF within the CBL was then calculated using

$$F = -\int_p^0 \frac{f}{g}\,dp \tag{3}$$

whereby f is the mean HMF between two dropsonde measurements, g is the gravitational acceleration as defined in equation (2), and dp is the difference in pressure between the two observations.

3. Large-Scale Meteorological Conditions

In order to better understand the processes that controlled the location, intensity, and other properties of the SHL on the day it was surveyed by the two aircraft, we first analyze (a) the spatial and temporal evolution of the SHL during the previous days and (b) the long-term climatological context of the SHL based on ERA-Interim reanalysis fields over the North African, European, and north-eastern Atlantic domain. The ERA-Interim reanalysis is used here as guidance only as significant errors may exist due to the scarcity of routine observations in the central western Sahara (Figure 1).

In the 5 days leading up to the 22 June 2011, a well-developed Azores High at 35°N/30°W slowly weakened before becoming reestablished on 22 June at 42°N/25 W in association with the ridge of a slowly moving westerly wave (Figures 2a–2f). Contemporaneous with the weakening of the Azores High over its climatological position in the subtropical north Atlantic, peak GPH_{500} values centered over southern Algeria at about 20°N on 18 June slowly migrated westward reaching the most western position centered over the Atlantic coast line at about 25°N on 22 June suggesting that large-scale subsidence-induced dry adiabatic heating may contribute to the increase in near-surface air temperatures over northern Mauritania from about 34–36°C on 17 June to above 38°C on 22 June (Figures 2a and 2f). The SHL as observed in the MSLP field migrated westward lagging slightly east of the center of GPH_{500} (Figure 2).

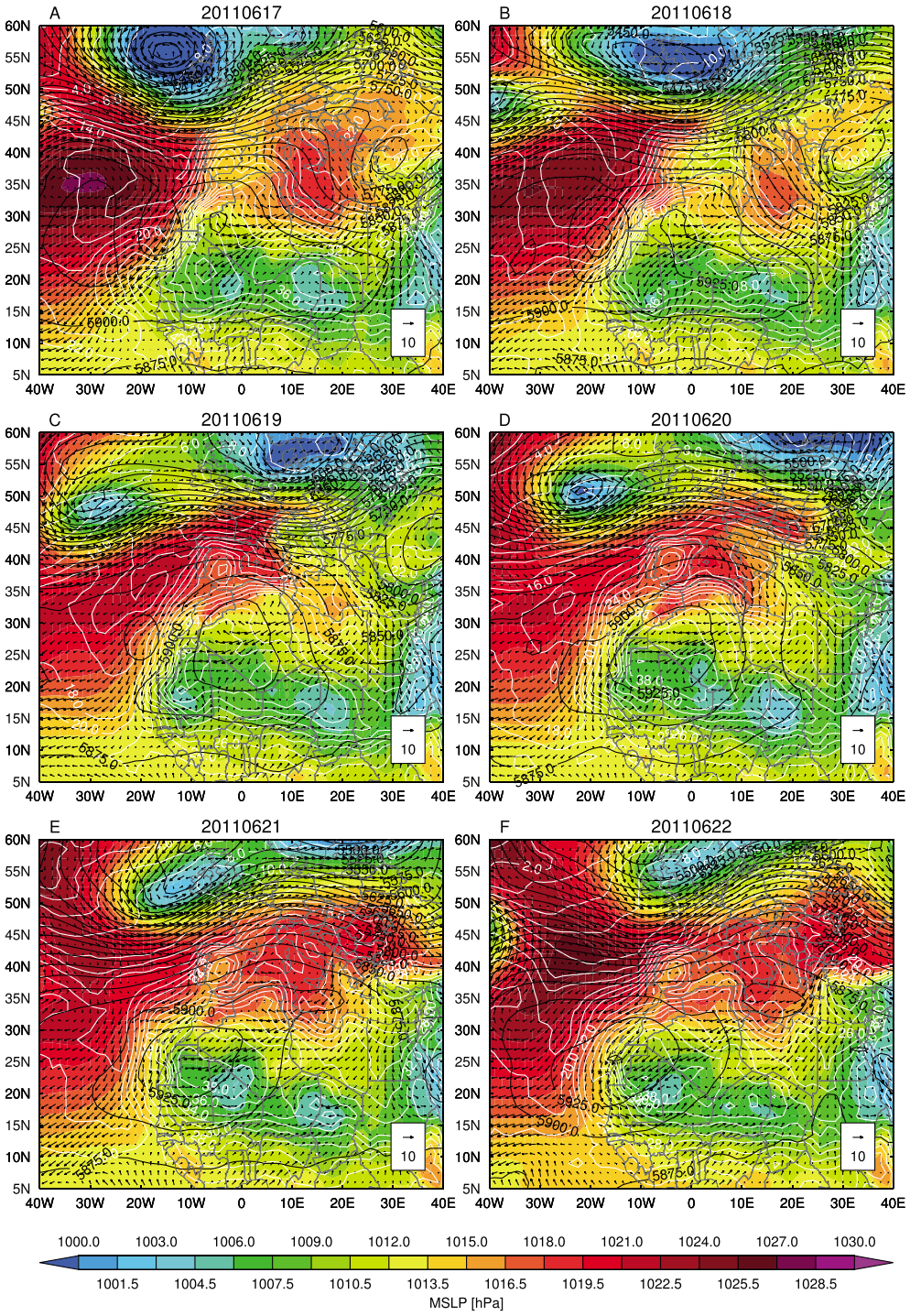

Figure 2. The 17–22 June 2011 ERA-Interim daily mean sea level pressure (color shading), 950 hPa air temperature (white contours), 500 hPa geopotential height (black contours), and 950 hPa wind vectors (black arrows). The reference wind vector is 10 m s^{-1}.

By 22 June 2011, the synoptic features over Europe, North Africa, and the tropical North Atlantic departed significantly from the climatological mean (Figures 3e and 3f). The Azores High was displaced northward, centered around 42°N and 22°W (Figure 3a). GPH_{500} and low-level air temperature maxima, climatologically located over southern Algeria (Figure 3c), were west-shifted over the Atlantic coast at about 25°N/15°W and northern Mauritania at about 22°N/10 W, respectively (Figure 3a). A well-defined

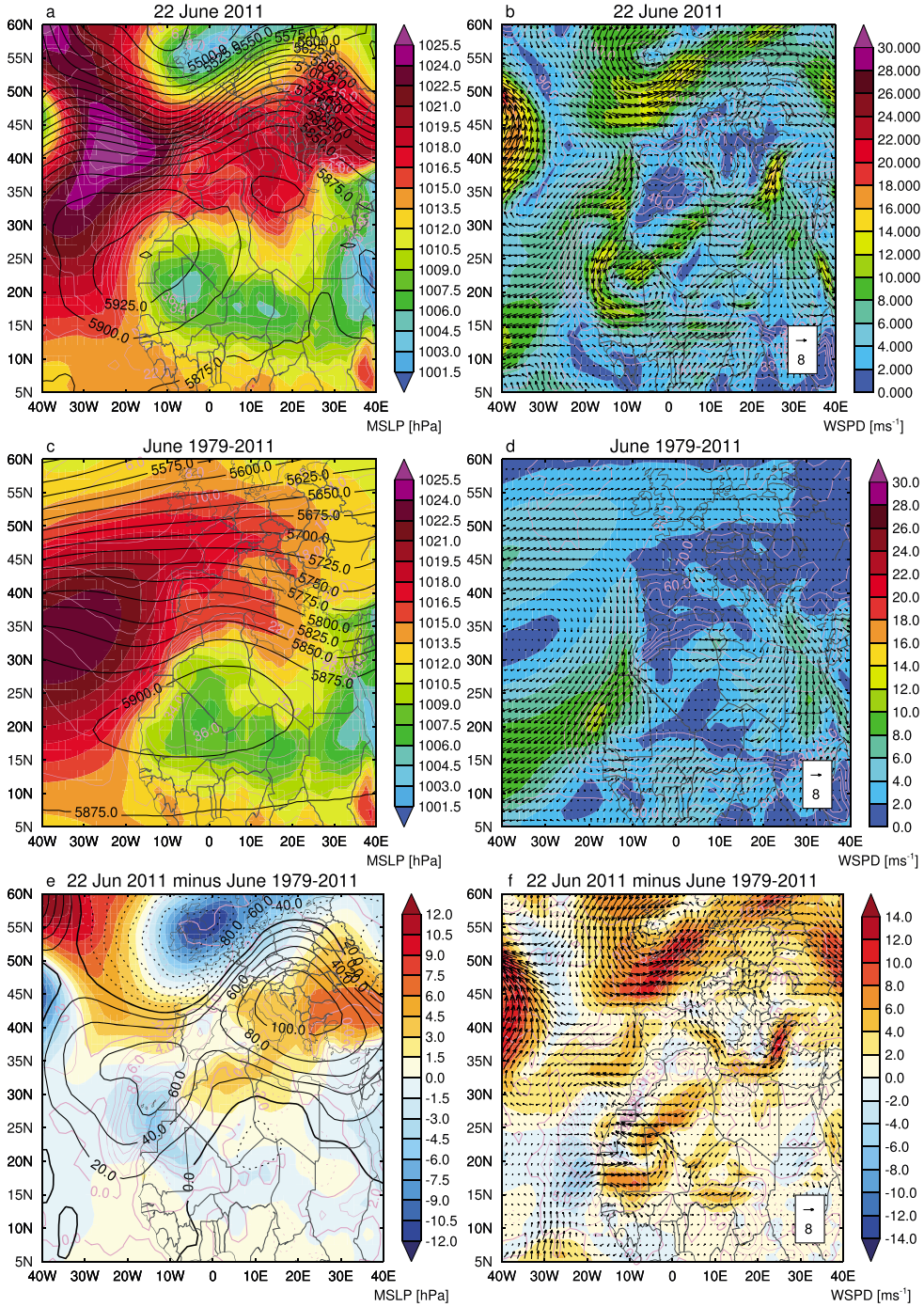

Figure 3. (a and b) Mean 22 June 2011, (c and d) mean 1979–2011 June, and (e and f) mean 22 June 2011 minus mean 1979–2011 June ERA-Interim climatology for mean sea-level pressure (color contour), 950 hPa air temperature (pink line contour) and 500 hPa geopotential height (black line contour) (Figures 3a, 3c, and 3e), and 950 hPa wind speed (color contour and vectors) and 950 hPa relative humidity (pink line contour) (Figures 3b, 3d, and 3f).

low-level cyclonic circulation (LLCC) around the heat low resulted in moist air inflow from the Atlantic recurving north into central Mali (Figure 3b). An anomalously strong northeasterly flow over central Algeria converged with Atlantic inflow at about 25°N over northern Mauritania (Figure 3b). MSLP was used in Figures 2 and 3 instead of LLAT because it also represents other large-scale features well such as the Azores High.

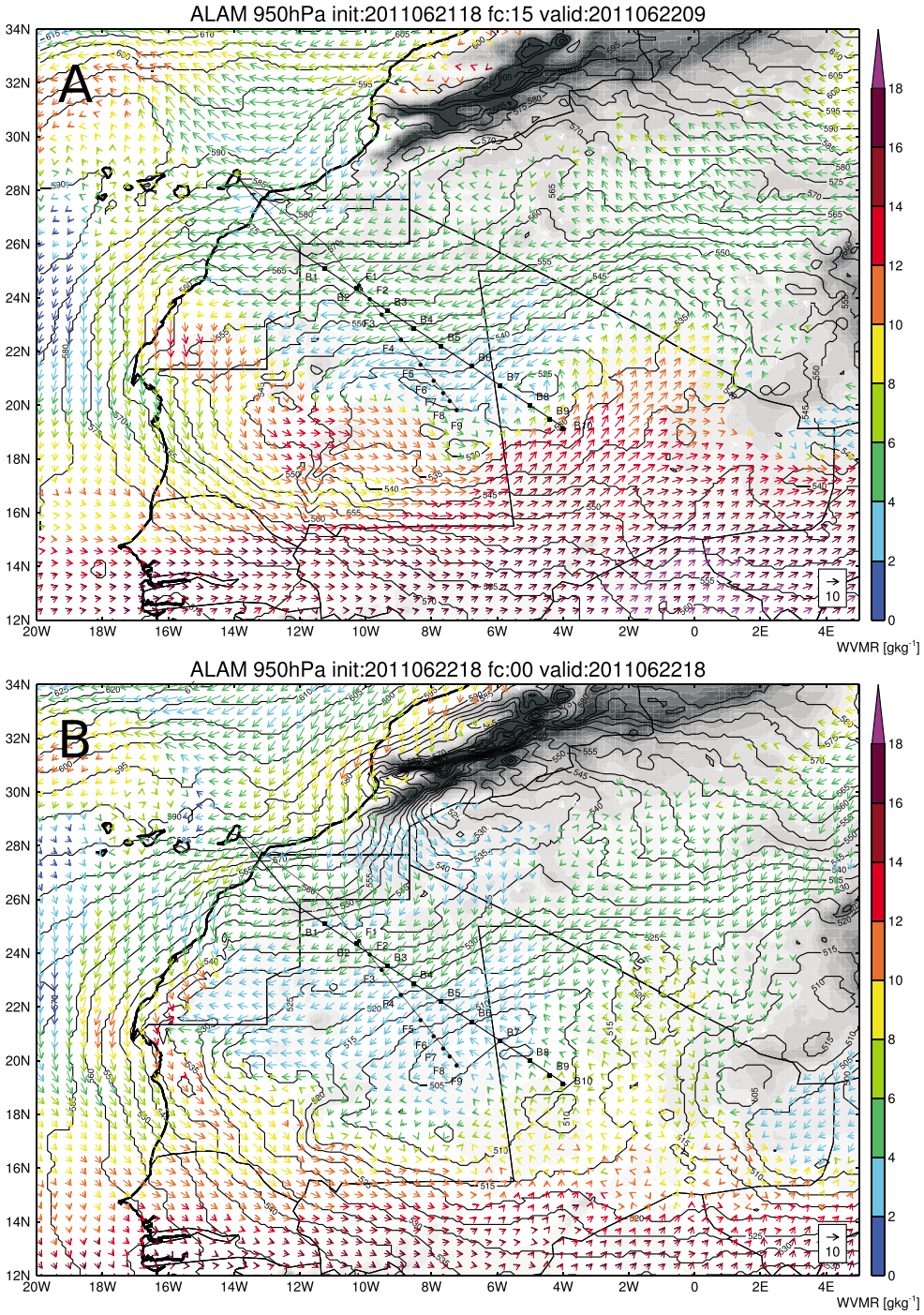

Figure 4. Africa-LAM forecast for 22 June 2011 (a) at 9 UTC initiated at 21 June 2011 at 18 UTC and (b) at 18 UTC initiated at 22 June 2011 at 18 UTC showing 950 hPa geopotential height (black line contours), wind direction and strength (arrow length), and water vapor mixing ration (WVMR, color of arrows). Filled grey contours indicate topography at 100 m intervals starting at 300 m above MSL (topography above 1400 m above MSL is one color). The flight tracks and dropsonde locations are marked for the BAe146 (filled squares) and F-20 (filled circles).

The position of the SHL on 22 June 2011 provided a unique opportunity within the Fennec Intensive Observation Period (IOP) to sample the Saharan troposphere since the SHL moved within the operating range of the two research aircraft. Note that we sampled the SHL on a day when it was about 5° east of its climatological mean position (Figures 3a and 3b). On no other day during the Fennec 2011 IOP we were

able to sample the SHL core region. Due to the lack of comparable flights, we are unable to evaluate how representative the SHL observations from 22 June 2011 are with respect to average SHL conditions.

4. The Saharan Heat Low on 22 June 2011

The flight planning of the 22 June 2011 Fennec SHL transects was guided by Africa-LAM forecasts initialized at 18 UTC the previous day. The flights targeted the SHL core region that in the 9 UTC GPH_{950} forecast field was located about 1.5° east of the Mauritania-Mali border at 21°N (Figure 4a), whereas in the previous 18 UTC analysis, the SHL core had an elongated shape with a NE-SW orientation crossing the border from Mali into Mauritania (Figure 4b). A consequence of the peculiar SHL shape forecast was that the aircraft with the shorter endurance (F20) was sent to sample the southern part of the SHL and the aircraft with the greater endurance (BAe146) was sent to sample the northern part of the SHL. In the forecasts, moist monsoon air is transported north into northern Mali and southern Algeria by the eastern branch of the LLCC which is especially pronounced in the 9 UTC forecast with 950 hPa wind speed ($WSPD_{950}$) in excess of $10\,m\,s^{-1}$ at around 4°W/17°N (Figure 4a). In the following two subsections we discuss in detail the dropsonde observations recovered from the flights into the SHL core region with respect to the SHL temperature-pressure configuration and atmospheric circulation (section 4.1) and the moisture transport in the SHL region (section 4.2).

4.1. Observed SHL and Atmospheric Circulation

To study the observed SHL characteristics, we use LLAT (see section 2.3 for details) as defined by *Lavaysse et al*. [2009] who showed that the difference between GPH_{700} and GPH_{950} is a useful metric for the identification of the SHL, larger LLAT values indicating a deeper, more intense SHL. In the morning, LLAT values range between 2668.5 and 2696.2 m including both flight tracks (Figures 5a and 5c). Two distinct local LLAT maxima were observed along the BAe146 track at B3 and B7 with corresponding LLAT maxima at F3 and F7 along the F-20 track. The eastern local maxima at B7 and F7 showing the largest LLAT of 2692.2 and 2695.3 m, respectively, correspond well with the expected location of the SHL based on the Africa-LAM forecasts (Figure 4). The secondary local LLAT maxima at B3 and F3 shows somewhat lower values of up to 2691.3 and 2690.7 m, respectively (Figures 5a and 5c). The LLAT increased in the afternoon in comparison to the morning, now ranging between 2679.9 and 2710.4 m including both flight tracks (Figures 5a and 5c). Both local LLAT maxima are still evident along both flight tracks (no F7 measurement available in afternoon but F8 instead, Figure 5c). The LLAT maxima associated with the SHL increased by 12.1 m to 2707.9 m at B7 and by 32.2 m to 2710.4 m at F7/F8. While the secondary LLAT maxima also increased in comparison to the morning at B3 and F3, the LLAT maxima here remain lower than in the SHL core region by 2.3 and 5.3 m, respectively. In both the morning and afternoon observations, the LLAT at F7/F8 is larger than that at B7 by 3.1 and 2.5 m, respectively (Figures 5a and 5c). When locating the longitudinal position of the SHL core region in the morning and afternoon on the respective BAe146 and F-20 flight tracks in Figure 1, it becomes evident that the SHL has an elongated shape stretching from northeast to southwest quite comparable to the Africa-LAM afternoon forecast (see dropsonde locations B7 and F7/F8 in Figure 4).

The LLAT maxima associated with the SHL core at B7 and F7/F8 are matched by local 950 hPa air temperature (T_{950}) maxima which show an increase from 40.1°C in the morning to 42.8°C in the afternoon along the F-20 flight track and a local afternoon maximum of 42.2°C along the BAe146 flight track (Figures 5b and 5d). In contrast, a local T_{950} minimum of 36.4°C observed at B7 in the morning is associated with the monsoon surge which brings colder air in this region (discussed in more detail in section 4.2). The surface heating and associated intensification of the SHL during daytime results in a well-defined SHL in the afternoon at B7 in the BAe146 data (Figure 5a). While the SHL core is matched by corresponding T_{950} maxima (except at B7 in the morning) as well as GPH_{950} minima (not shown), the western LLAT maxima at B3 and F3 do not show a matching pattern in T_{950} and GPH_{950} indicating that the increased LLAT here is the result of increased GPH_{700}.

The spatial pressure differences associated with the SHL development and its geographic location are expected to have a significant control on the large-scale atmospheric circulation. In the morning a southerly wind of $5.2\,m\,s^{-1}$ at 950 hPa was observed at the most eastern sonde location B8 (Figure 5e)

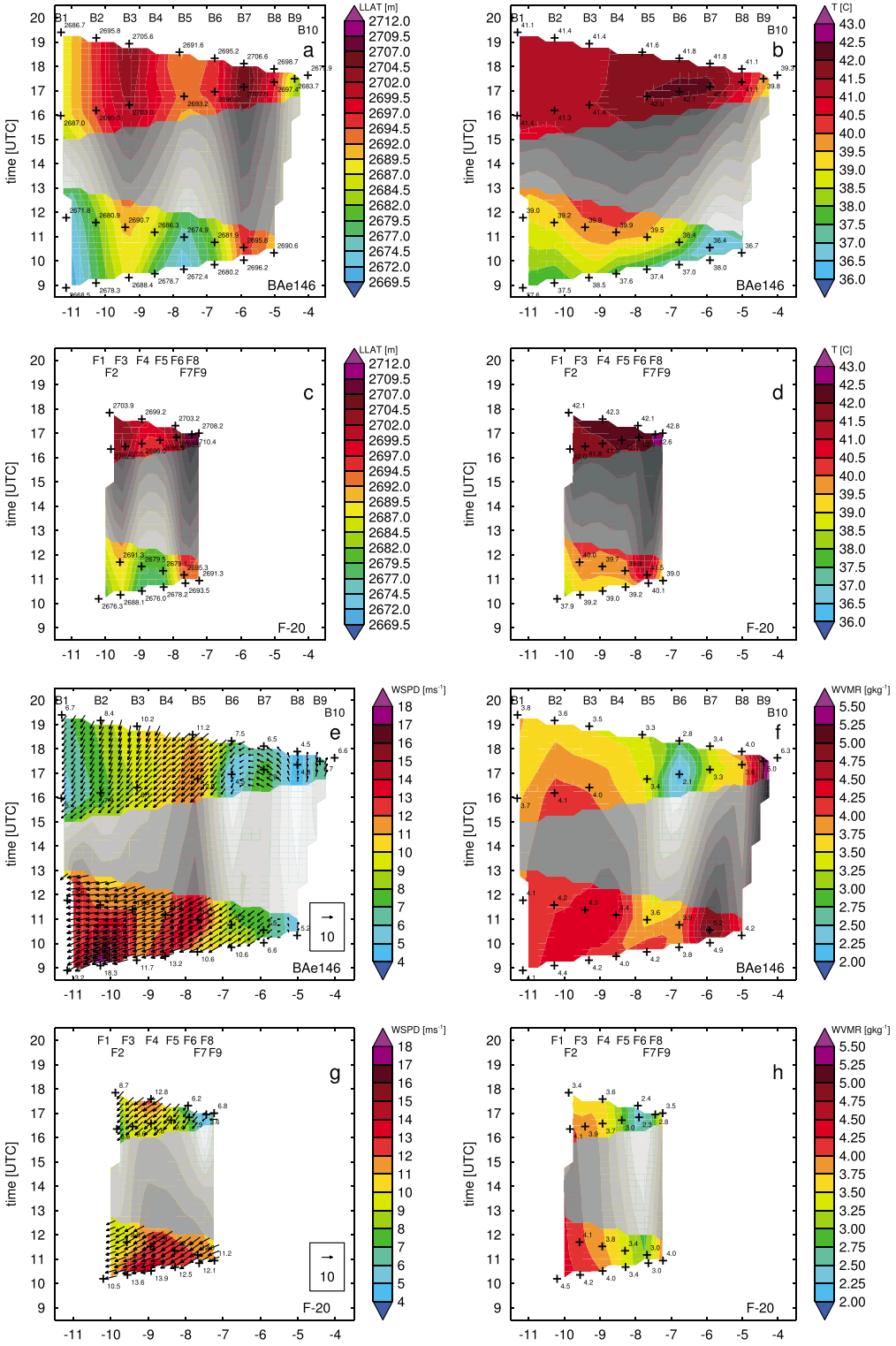

Figure 5. Hovmöller plots (longitude by time) of BAe146 and F-20 dropsonde-derived low-level atmospheric thickness defined as the difference between (a and c) 700 and 950 hPa geopotential height, (b and d) air temperature, (e and g) wind speed and direction, and (f and h) water vapor mixing ratio at 950 hPa on 22 June 2011. Dropsonde locations are indicated by plus symbols and labeled at the top of each plot. The greyed out contour lines mark the region between the morning and afternoon flights where the temporal interpolation may not be trusted as the time difference is quite large.

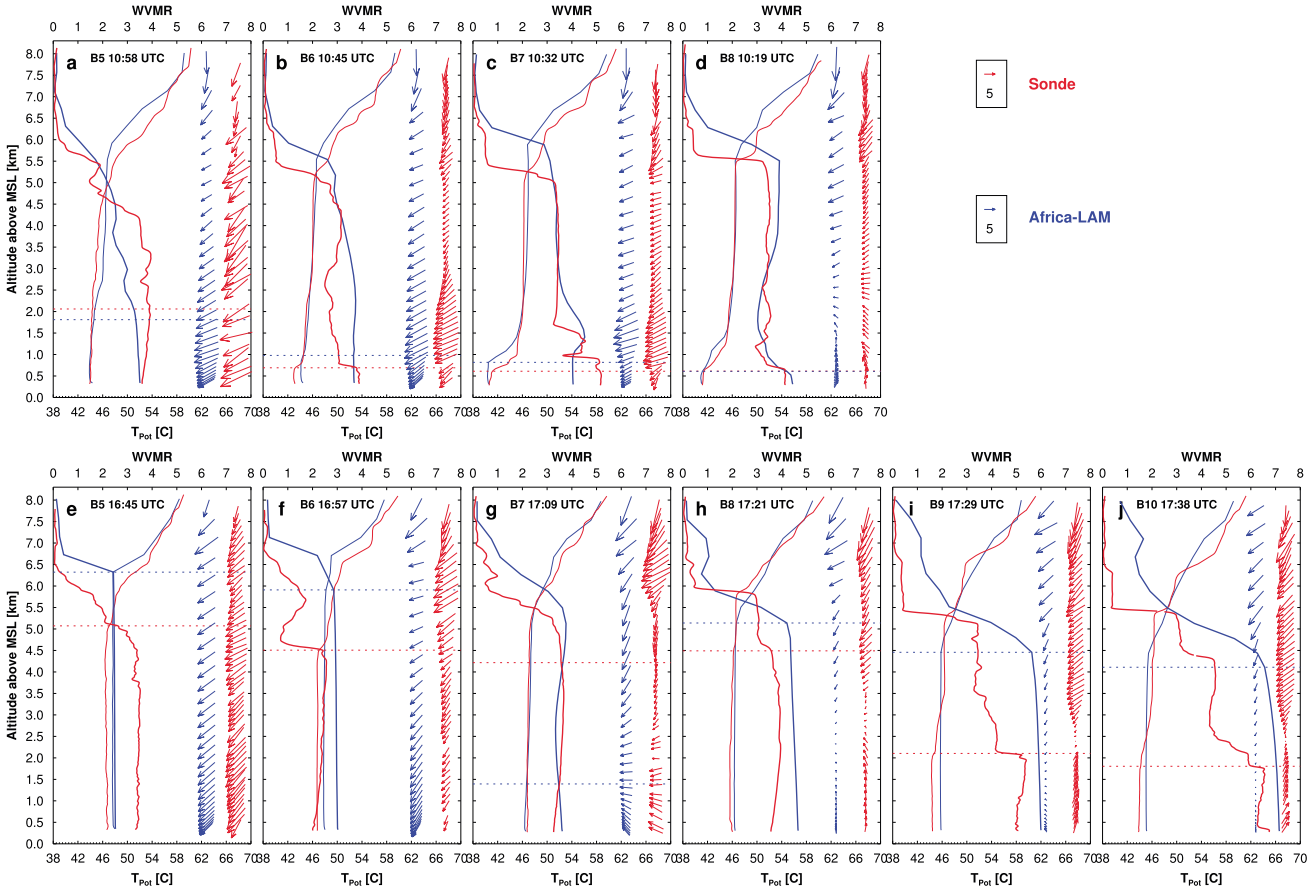

Figure 6. BAe146 (red) dropsonde and corresponding Africa-LAM (blue) profiles of water vapor mixing ratio (WVMR, thick solid line, top axis), potential temperature (T_{pot}, thin solid line, bottom axis), and horizontal wind speed and direction (vectors) derived for locations (a to d) B5 to B8 during the morning return flight and (e to j) B5 to B10 during the afternoon out-going flight. The reference wind speed vector shown in the top right is 5 m s^{-1}. The horizontal blue and red lines denote the top of the planetary boundary layer (see section 2.3 for how the boundary layer depth was determined).

showing that the aircraft sampled the western edge of the monsoon surge expected east of the SHL core (Figure 4a). A northeasterly wind of 6.6 and 7.5 m s^{-1} was observed at the next westward sonde location B7 that turns into an easterly wind farther west in both aircraft data. A similar change in wind direction can be observed in the afternoon along the eastward extended BAe146 track where southerly winds at B8 turn into northeasterlies toward B6 (Figure 5e). In both cases the aircraft observations very likely captured the LLCC around the northern part of the SHL as also evident in the Africa-LAM forecasts (Figure 4). $WSPD_{950}$ in excess of 10 m s^{-1} west of 7°W in both aircraft data in the morning and between 7° and 9°W in the afternoon are associated with the harmattan (Figures 5e and 5g) with a decline in speed over the day consistent with the breakdown of the morning LLJ. A local $WSPD_{950}$ maximum of 18.3 m s^{-1} was observed at B2 during the morning LLJ maximum.

4.2. Observed Moisture Transport in the SHL Region

During the morning flights, a local maximum in the 950 hPa water vapor mixing ratio ($WVMR_{950}$) up to 5.2 g kg^{-1} was observed along the BAe146 flight track at sonde location B7 (Figure 5f). The $WVMR_{950}$ decreases westward to a minimum as low as 3.6 g kg^{-1} at B5. We do not know if a $WVMR_{950}$ maximum similar to the BAe146 track exists east of about 7 W along the Falcon-20 track, but a $WVMR_{950}$ morning minimum of 3.0 g kg^{-1} was observed along the F-20 track at F7 (Figure 5h). Explaining this moisture distribution in the morning requires a closer look at the dropsonde profiles in which some very interesting structures emerge (which present challenges to the models; see section 5.2). The observed morning WVMR and T_{pot} profile at B5 shows fairly constant values around 3.7 g kg^{-1} and 44°C up to about 2.0 km (Figure 6a).

The profiles farther east at B6, B7, and B8 show a distinct near-surface moist layer varying in depth between about 0.6 and 0.9 km above MSL that in this geographic setting one would likely associate with the monsoon and a deep, dry well mixed, presumably residual Saharan layer above to ~4.5–5 km (Figures 6b–6d). The developing morning CBL at B7 is very shallow reaching up to about 0.6 km above MSL, whereas the near-surface moist layer reaches up to about 0.8 km above MSL indicating that this distinct moist layer was present already before the CBL growth started (Figure 6c). At the most eastern sonde location B8, the winds associated with the low-level moist layer are indeed southerlies (Figure 5e) indicating the location of the monsoon surge expected east of the SHL core. However, at B6 and B7 the winds associated with the near-surface moist layer are northeastly (Figures 6b and 6c). The change in wind direction combined with our understanding of the monsoon and SHL system suggests that the near-surface moist layers observed at B6 to B8 are the result of moist monsoon air being transported around the SHL core in the LLCC northern branch. This hypothesis is supported by the Africa-LAM morning forecast which shows cyclonic moisture transport in the flow north of the SHL core resulting in increased $WVMR_{950}$ between 4 and 6 g kg^{-1} in the northeasterly flow close to B7 (Figure 4a). The morning moisture distribution in the SHL region is further complicated by a second moist layer observed above the CBL between 1 and 1.5 km above MSL at B7 that shows $WVMR_{950}$ values up to about 4.5 g kg^{-1} and northeasterly winds (Figure 6c).

Afternoon $WVMR_{950}$ values are lower than in the morning at all F-20 track sonde locations and at BAe146 sonde locations B1 to B8 which in parts can be explained by the increased afternoon CBL depth and associated vertical mixing of moisture (Figures 5f and 5h).

Only at the two most eastern sonde locations B9 and B10 which were not sampled in the morning high $WVMR_{950}$ values of 5.0 and 6.3 g kg^{-1}, respectively, were observed. Associated with southerly winds, these are likely the result of the monsoon surge core region (Figures 5e and 5f). The moist monsoon layer at B9 and B10 is about 2.1 and 1.8 km deep, respectively, with WVMR values at B10 in excess of 6 g kg^{-1} (Figure 6j). It is not possible to say whether higher WVMR values existed in the B9 to B10 region in the morning due to the lack of observations here. The top of the CBL at B7 and B8 increased from about 0.6 km to about 4.2 and 4.5 km above MSL suggesting that any moisture transported into this region would be mixed in the deep CBL by the afternoon (Figure 6). This would also explain the lack of any afternoon near-surface moist layer at B6 to B8 as observed in the morning. However, it cannot be ruled out that a westward displacement of the lower atmospheric levels of the SHL occurred between the morning and afternoon, as indicated by the $WSPD_{950}$ observations (Figure 5e), which would have an impact on the geographic location, main direction, and strength of the monsoon surge. The LLCC north of the SHL core is still present in the afternoon dropsonde observations. The local moisture minimum identified along both flight tracks in the morning intensifies toward the afternoon reaching $WVMR_{950}$ values as low as 2.3 g kg^{-1} at F6 and 2.1 g kg^{-1} at B6 (Figures 5f and 5h). These very dry regions in the afternoon seem to be associated with the SHL core region (Figures 5a and 5c).

The evaluation of NWP and climate models is one of the main objectives of the Fennec program. In the following section we will evaluate how well the UK Meteorological Office Limited Area Model set up over the northern Africa domain (Africa-LAM) was able to forecast the observed SHL and its properties.

5. Africa-LAM Evaluation

5.1. Forecast SHL and Atmospheric Circulation

High LLAT up to 2691.3 and 2690.1 m indicate the location of the SHL at sonde locations B6/B7 and F7, respectively (Figures 7a and 7c). Similar to the observations, the Africa-LAM shows a small increase in LLAT up to 2689.9 m at sonde location B3, but the difference to the neighboring sonde locations B2 and B4 are only 1 to 2 m (Figure 7a). A distinct local LLAT maximum as in the sonde data cannot be observed at F3 (Figure 7c). In the SHL region the model underestimates LLAT along both the BAe146 and F-20 flight track by up to 6.9 and 5.2 m, respectively (Figures 8a and 8c). Similarly, the local maxima at B3 and F3 are underestimated by up to 5.7 and 3.3 m, respectively. Elsewhere the model mainly overestimates LLAT in the morning by up to 16.6 and 10.5 m along the BAe146 and F-20 flight track, respectively.

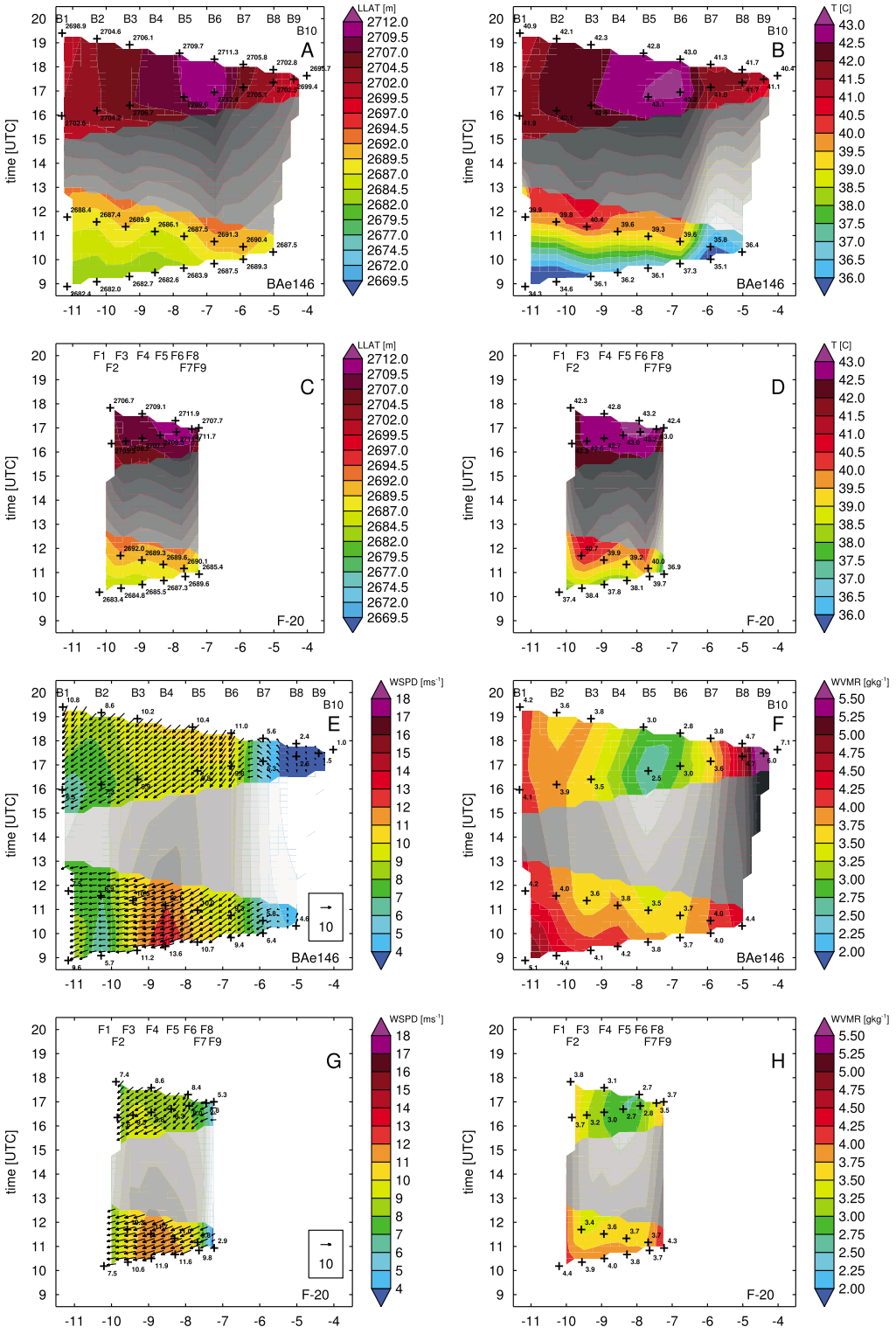

Figure 7. Hovmöller plots (longitude by time) of Africa-LAM forecasts interpolated to BAe146 and F-20 dropsonde locations and times showing low-level atmospheric thickness defined as the difference between (a and c) 700 and 950 hPa geopotential height, (b and d) 950 hPa air temperature, (e and g) 950 hPa wind speed and direction, and (f and h) 950 hPa water vapor mixing ratio on 22 June 2011. Dropsonde locations are indicated by plus symbols and labeled at the top of each plot. The greyed out contour lines mark the region between the morning and afternoon flights where the temporal interpolation may not be trusted as the time difference is quite large.

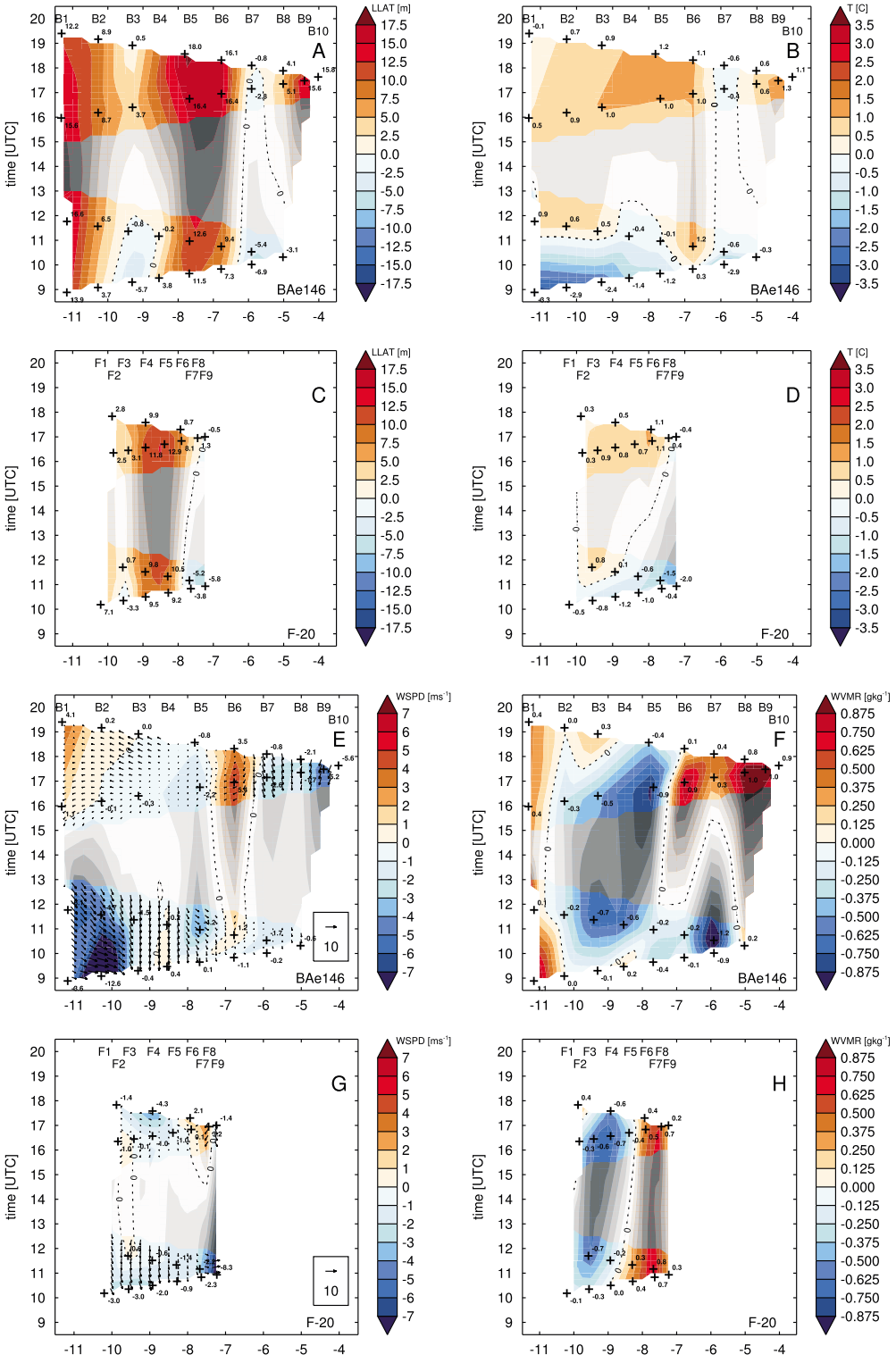

Figure 8. Hovmöller plots showing difference (model minus observations) between BAe146 and F-20 dropsonde measurements (Figure 5) and interpolated Africa-LAM forecasts (Figure 7) of low-level atmospheric thickness defined as the difference between (a and c) 700 and 950 hPa geopotential height, (b and d) air temperature, (e and g) wind speed and direction, and (f and h) water vapor mixing ratio on 22 June 2011. Dropsonde locations are indicated by plus symbols and labeled at the top of each plot. The greyed out contour lines mark the region between the morning and afternoon flights where the temporal interpolation may not be trusted as the time difference is quite large. The dotted line marks the zero line.

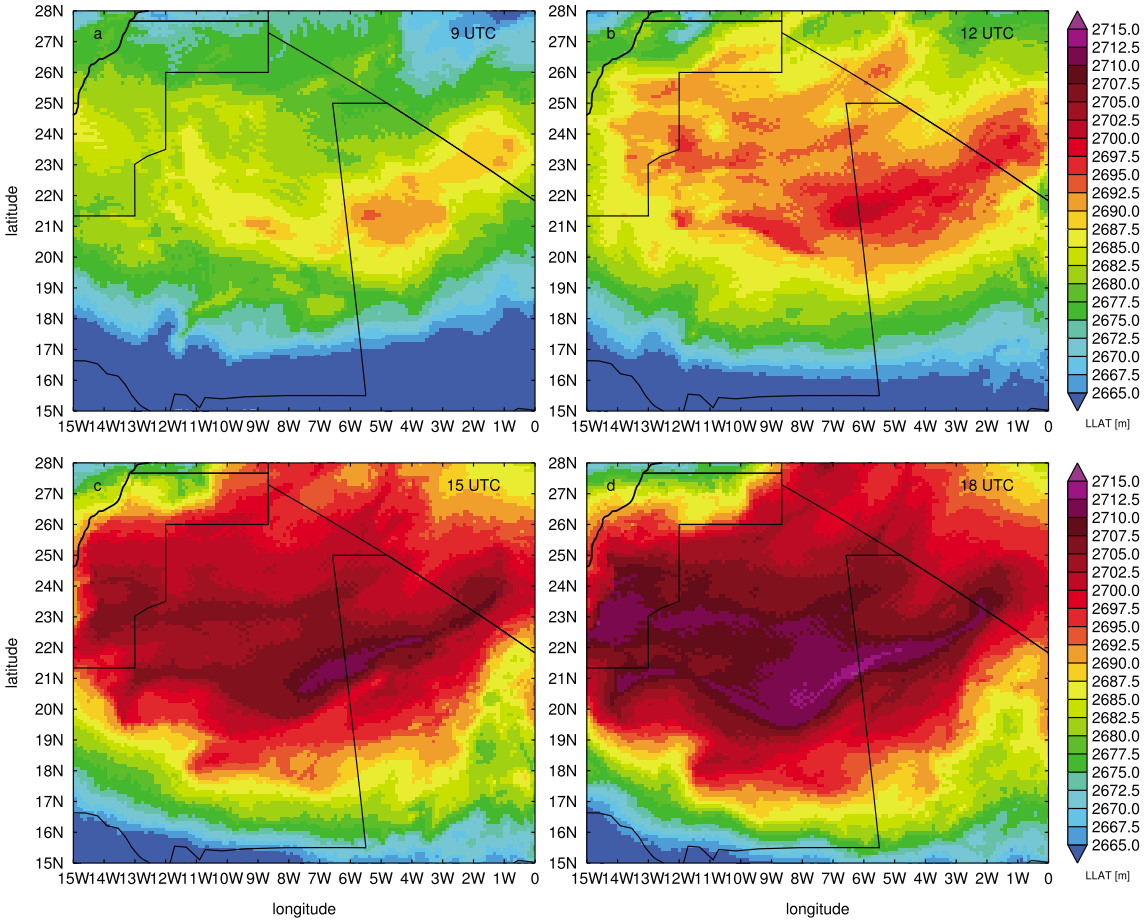

Figure 9. Africa-LAM low-level atmospheric thickness (LLAT) over the SHL region for (a) 9 UTC, (b) 12 UTC, (c) 15 UTC, and (d) 18 UTC. LLAT is calculated by subtracting 700 hPa from 950 hPa geopotential height following *Lavaysse et al.* [2009].

During the afternoon a well-developed SHL can be identified along both flight tracks with highest LLAT of 2712.4 and 2711.9 m at B6 and F6, respectively (Figures 7a and 7c). This puts the afternoon SHL core region about 0.5 to 1.0° farther west in the model compared to the observations. The observed afternoon local LLAT maxima at B3 and F3 are not evident in the Africa-LAM data. The afternoon SHL core appears less deep and more spatially stretched in the model missing an increasing LLAT gradient toward the SHL core as evident in the observations between B6 and B8 (Figure 5a). The overestimation of LLAT in the model increases in the afternoon reaching differences up to 18.0 m at B5 and 11.8 m at F4 in comparison to the observations (Figures 8a and 8c). Only in the SHL core region the model underestimation of LLAT is reduced to 2.8 and 0.5 at B7 and F9, respectively, which in the latter case is smaller than the observational LLAT error of ±1 m (Figures 8a and 8c). This LLAT underestimation is like the result of the less pronounced representation of the SHL in the model. The model shows a NE-SW orientation similar to the observations in the morning as well as in the afternoon.

While the Africa-LAM LLAT interpolation to the sonde locations and release times (Figures 7a and 7c) is the closest comparison possible, it does not allow for an evaluation of how the SHL evolves in the model's own spatial and temporal domain. Therefore, we here include a brief analysis of Africa-LAM LLAT on the model's own grid (Figure 9). In the morning the Africa-LAM shows the SHL core centered around at 21°N and 5.5°W at 9 UTC and 6°W at 12 UTC (Figures 9a and 9b). From 12 UTC on the SHL, core region starts stretching in a NE-SW direction with the core region remaining over the Algeria-Mali border at about 21°N creating a rather complex SHL structure by 18 UTC (Figure 9d). Throughout the day the maximum LLAT associated with the SHL core increases from 2695 m at 9 UTC to about 2715 m at 18 UTC (Figure 9).

The Africa-LAM forecasts capture the overall T_{950} distribution well with an expected increase in temperature during daytime and a local afternoon maximum up to 43.2°C at B6 and F6 (Figures 7b and 7d). Similar to the observations, the model shows cooler temperatures as low as 35.1°C at the most eastern sonde locations B7 and B8 in the morning suggesting that in the model the SHL core region is also influenced by colder monsoon air (Figure 7b). Until about 11 UTC, the model underestimates T_{950} (exception at B6 during morning return flight) by up to 3.3°C (most western sonde location B1), whereas it mainly overestimates T_{950} for the rest of the day by up to 1.3°C at B9 with some exceptions, for instance, at B7 (Figures 8b and 8d). In the model, the T_{950} maximum agrees well with the LLAT maximum along the BAe146 flight track but both are offset westward by about 1° compared to the observations (Figures 5a, 5b, 7a, and 7b).

The Africa-LAM forecasts the large-scale wind regime well, but differences exist in the absolute magnitudes of the $WSPD_{950}$ compared to the observations. With some minor exceptions at B4, B6, and F3, the Africa-LAM underestimates morning wind speed at all sonde locations (Figures 8e and 8g). The underestimation is especially large at the most eastern F-20 sonde location F9 ($-8.3\,m\,s^{-1}$) and at B2 ($-12.6\,m\,s^{-1}$). The latter is the result of the local maximum of $18.3\,m\,s^{-1}$ observed at B2 in the morning that is not represented in the model suggesting that this single high wind speed observation may have been caused by a local low-level jet (LLJ) not simulated or displaced in the model ($WSPD_{950}$ underestimated in model by $12.6\,m\,s^{-1}$, Figure 8e). This hypothesis is supported by two additional facts: first, the time of the B2 dropsonde observation at 9:05 UTC corresponds well to the peak time at which momentum from LLJs tends to mix down in the Sahara as a result of increasing morning dry convection after sun rise [*May*, 1995; *Schepanski et al.*, 2009; *Allen and Washington*, 2014], and second, the relatively low wind speed of $11.6\,m\,s^{-1}$ measured at 11:34 UTC during the return leg corresponds to the short-lived nature of LLJs. The geographic location of the monsoon surge in the model matches the observations well with southerly winds at B8 both in the morning and afternoon (Figures 5e and 7e). The monsoon surge $WSPD_{950}$ is, however, underestimated by the model. $WSDP_{950}$ at the most eastern sonde locations B9 and B10 is underestimated by up to $5.6\,m\,s^{-1}$ (Figure 8e). Some differences exist between the model and observations associated with the change in wind direction from southerly (B8) to southeasterly (B7) to northeasterly (B6) in that the pronounced increase in $WSPD_{950}$ westward toward the harmattan flow occurs in the model between B6 and B7 and in the observations between B5 and B6 (Figures 5e and 7e). This displacement leads to a model $WSPD_{950}$ overestimation at B6 and underestimation at B5 (Figure 8e).

5.2. Forecast Moisture Transport in the SHL Region

Increased $WVMR_{950}$ observed at B7 in the morning associated with the near-surface moisture transport in the LLCC (see section 4.2) is underestimated by 1.2 $g\,kg^{-1}$ in the model. The $WVMR_{950}$ levels in the harmattan flow are generally underestimated by the model along both flight tracks by up to 0.9 $g\,kg^{-1}$ (Figures 8f and 8h). Despite the model underestimating afternoon wind speed in the monsoon surge region (B8 to B10), it overestimates $WVMR_{950}$ here by up to 1 $g\,kg^{-1}$ (Figure 8f). The $WVMR_{950}$ minima observed along the F-20 morning and afternoon track as well as the BAe146 afternoon track are displaced westward by about 1 to 2° in the Africa-LAM forecasts leading to a dipole in the difference plots (Figures 8f and 8h).

The observed and simulated atmospheric profiles show that the Africa-LAM captures the morning near-surface moisture level and depth of the northward monsoon surge at B8 well (Figure 6d), but it struggles to simulate the low-level moisture transport around the SHL core in the LLCC correctly (Figures 6b and 6c). At B7 the 1 km deep observed near-surface moist layer is not well defined in the model and its magnitude of about 4.2 $g\,kg^{-1}$ is underestimated by about 1 $g\,kg^{-1}$ (Figure 6c). Interestingly, the model seems to capture the secondary layer observed between about 1 and 1.7 km above MSL, although the upper and lower boundaries of this layer are not well defined. It should be noted that the simulated CBL at B7 is about 0.25 km deeper than the observed CBL suggesting a deeper vertical mixing of moisture in the model: this aspect is discussed in more detail in section 5.3. At B6 the distinct near-surface moist layer observed in the morning cannot be identified in the Africa-LAM forecast (Figure 6b).

Africa-LAM afternoon profiles show that moisture from the monsoon and LLCC near-surface moist layer observed in the morning is well mixed within a deep boundary layer at all sonde locations except at B7

where the simulated CBL top is at about 1.4 km above MSL (Figures 6e–6j). The simulated afternoon CBL depth in the monsoon inflow region at B9 and B10 of about 4.5 and 4.2 km above MSL, respectively, is more than twice as deep compared to the observations suggesting a much deeper vertical mixing of moisture in the model which is likely to impact the large-scale moisture distribution due to differing wind regimes below and above about 2.5 km above MSL (Figures 6i and 6j). The shallow simulated CBL reaching up to about 1.4 km at B7 is associated with stronger southeasterly winds of more than 5 m s^{-1} compared to low wind speeds of only up to 2 m s^{-1} at B8 to B10 suggests that at least part of the moisture flow in the northern branch of the LLCC is simulated by the model (Figure 6g).

The differences between the observed and simulated moisture fields and profiles indicate that the model is able to simulate the morning monsoon surge reasonably well but that it is limited in its ability to simulate the magnitude of near-surface moisture transport north of the SHL core correctly. In the afternoon the model mixes moisture transported north by the monsoon surge at B8 to B10 within a boundary layer up to about 4.2 km deep showing no distinct moist layer whereas the observations show a very distinct near-surface moist layer that corresponds to the shallower about 2.5 km deep CBL (e.g., Figure 6i). This result is consistent with the observational and modeling study of *Garcia-Carreras et al*. [2014], who have shown that entrainment into the Saharan CBL, which is capped by a near-neutral residual layer, is much weaker than (around one quarter of) that of classical convective boundary layers capped by a stable inversion and that models therefore overestimate the rate of boundary layer growth in the morning, for the Sahara.

5.3. Vertically Integrated Horizontal Moisture Flux in the CBL

With the development of the CBL in the morning, moisture will be vertically mixed between the surface and the CBL top. Therefore, an assessment of the observed and modeled CBL depth and the vertically integrated moisture flux within the CBL is critical to the evaluation of the moisture budget in the SHL region. The model matches the observed morning CBL depth reasonably well, only slightly overestimating the depth by about 0.4 and 0.3 km at B6 and B7 and underestimating the CBL top by about 0.2 km at B5; at B8 it is exactly the same as in the observations (Figure 10, horizontal dashed lines). The difference between the observed and simulated magnitude of the vertically integrated horizontal moisture flux (HMF) of 5 and 8 g m kg^{-1} s^{-1} at B7 and B8, respectively, is small and likely to be within the uncertainties associated with the vertically integrated HMF calculation (Figures 10k and 10l). The relatively small difference in vertically integrated HMF at B7 of only 5 g m kg^{-1} s^{-1} (Figure 10k) suggests that the ~0.2 km deeper CBL in the model is enough to compensate for the underestimation of WVMR by about 1 g kg^{-1} in the observed near-surface moist layer (Figure 6c). The observed near-surface moist layer at B7 is clearly evident in the meridional component of the moisture flux up to about 0.7 km above MSL (Figure 10g), whereas moisture above the CBL including the elevated moist layer is more pronounced in the zonal component between 0.7 and 1.5 km above MSL (Figure 10c) indicating different transport regimes in the CBL and above. At B6, B7, and B8, the vertically integrated HMF profiles match the observations well, although the simulated profile at B7 appears shifted upward by about 0.5 km. Only at B5 does the model strongly underestimate the zonal and meridional HMF by up to 40 g m kg^{-1} s^{-1} (Figures 10a and 10e).

In the afternoon the magnitude of the observed vertically integrated HMF ranges between 299 at B8 and 1600 g m kg^{-1} s^{-1} at B5 with all values being larger than in the model except at B6 where the simulated vertically integrated HMF of 1129 g m kg^{-1} s^{-1} is more than twice that of the observations (Figures 11m to 11r). In the monsoon surge core region at B9 and B10, the observed vertically integrated HMF is about twice that in the model (596 and 585 g m kg^{-1} s^{-1}, respectively) despite the CBL in the model being more than twice as deep as in the observations (about 4.5 and 4.1 km above MSL, respectively; B9 and B10 in Figure 11). This is the result of two factors. First, up to about 2 km above MSL the model wind speed is almost an order of magnitude lower than observed resulting in HMF values below 10 g m kg^{-1} s^{-1} compared to between 30 and 40 g m kg^{-1} s^{-1} in the observations (Figures 11q and 11r). Second, the meridional component of the simulated HMF at B7 to B10 is positive in the lower troposphere up to about 2.5 km above MSL compared to up to 3.0 km above MSL in the observations, whereas it is negative above which results in vertically integrated meridional HMF values as low as −40 g m kg^{-1} s^{-1} in the model (Figures 11i to 11l).

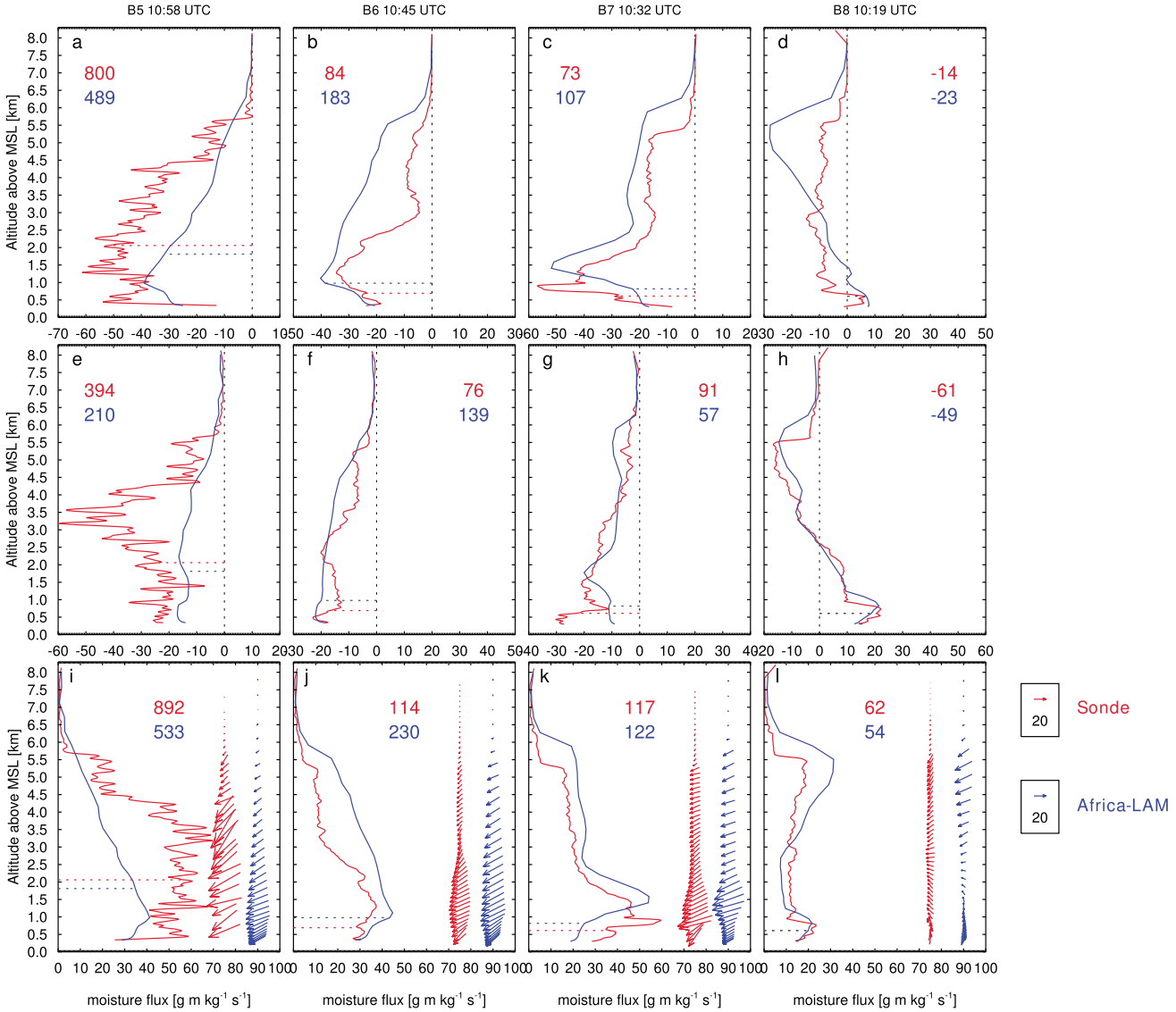

Figure 10. BAe146 (red) dropsonde and corresponding Africa-LAM (blue) profiles of horizontal moisture flux at B5 to B8 for the morning return flight showing the (a–d) u-component, (e–h) v-component, and (i–l) magnitude. The red and blue numbers in each panel show the vertically integrated horizontal moisture flux (VIHMF) between the surface and the top of the CBL (horizontal dotted line) for the observations and model, respectively. The reference horizontal moisture flux vector shown in the top right is 20 g m kg^{-1} s^{-1}.

The more than twice as deep simulated CBL in the monsoon surge region in the afternoon has a critical impact on the moisture transport pathways in the model as a result of differing wind directions below and above about 2.5 km above MSL (Figures 11q and 11r). Whereas the observed shallow CBL facilitates moisture transport toward the north and northeast only, moisture in the model is mixed more than twice as deep and transport here is toward north to northwest in the lower part of the CBL and toward the southwest in the upper part of the CBL (Figures 6i and 6j and Figures 11q and 11r). This is likely the most important difference between the model and observations in this study as it demonstrates that the CBL depth not only controls the depth over which moisture is vertically mixed but more importantly controls to which parts of the central Sahara moisture is transported. This is critical for convection-associated dust emission events [e.g., *Allen et al.*, 2013; *Marsham et al.*, 2013]. While explicit convection schemes are necessary for model simulation of cold pool outflows [e.g., *Marsham et al.*, 2011; *Solomos et al.*, 2012], if moisture is transported to regions different to observed to begin with, then even these model configurations could struggle.

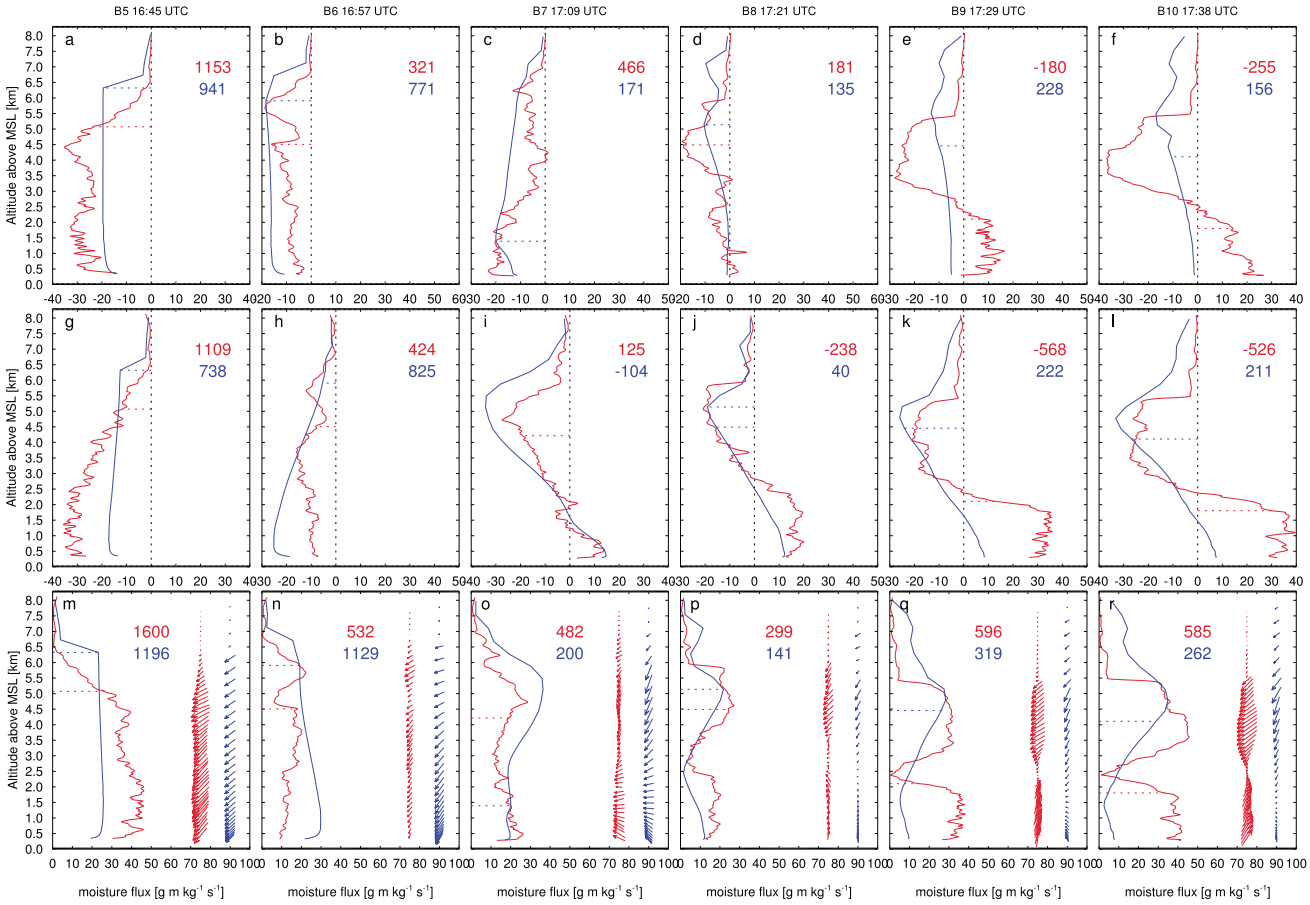

Figure 11. Same as Figure 10 but for the afternoon outgoing flight at sonde locations B5 to B10.

6. Discussion

Having two aircraft dropping sondes simultaneously on different tracks allows analysis of the state of the atmosphere in three spatial dimensions, with temporal sampling giving four daytime soundings at a number of dropsonde positions. For instance, with only a single aircraft it would have been impossible to capture the location of the SHL core or to verify that the SHL has an elongated shape with a northeast-southwest orientation. While the observed location of the SHL core identified in the LLAT field does not change between morning and afternoon (Figures 5a and 5c), the LLCC observed in the $WSPD_{950}$ field (Figure 5e) and GPH_{950} field (not shown) indicates that the SHL core at lower altitude may have moved westward between the morning and afternoon by about 1°. This agrees well with the general movement of the SHL from east to west in the preceding days as seen in the ERA-Interim reanalysis (Figure 2). This SHL migration persists in the following days until it reaches its most western position at 6°W and 22°N on 23 June 2011 [*Flamant et al.*, 2012].

In the long-term mean, the SHL takes a central geographic position in the western Sahara where it draws in dry harmattan air in the north, moist air from the Atlantic in the west, and the monsoon in the south (Figures 3c and 3d). Understanding the variability and characteristics of the moisture transport pathways is essential for our understanding of convective processes and associated dust emission as a result of cold pool outflow in the central Sahara. Cold pools themselves have also been observed as a mechanism for moisture transport into the Sahara [e.g., *Flamant et al.*, 2009] having the potential to initiate new convection which can spawn additional cold pools. On 22 June 2011, the SHL is located about 5° west and 4° south from its climatological mean position (Figure 3). As a result the monsoon surge is being fed primarily by moist air from the western Mauritanian coast (Figure 3b). The role of the SHL in providing a mechanism for monsoon surges into the central Sahara has been noted before [*Parker et al.*, 2005; *Cuesta et al.*, 2010; *Allen and Washington*, 2014]

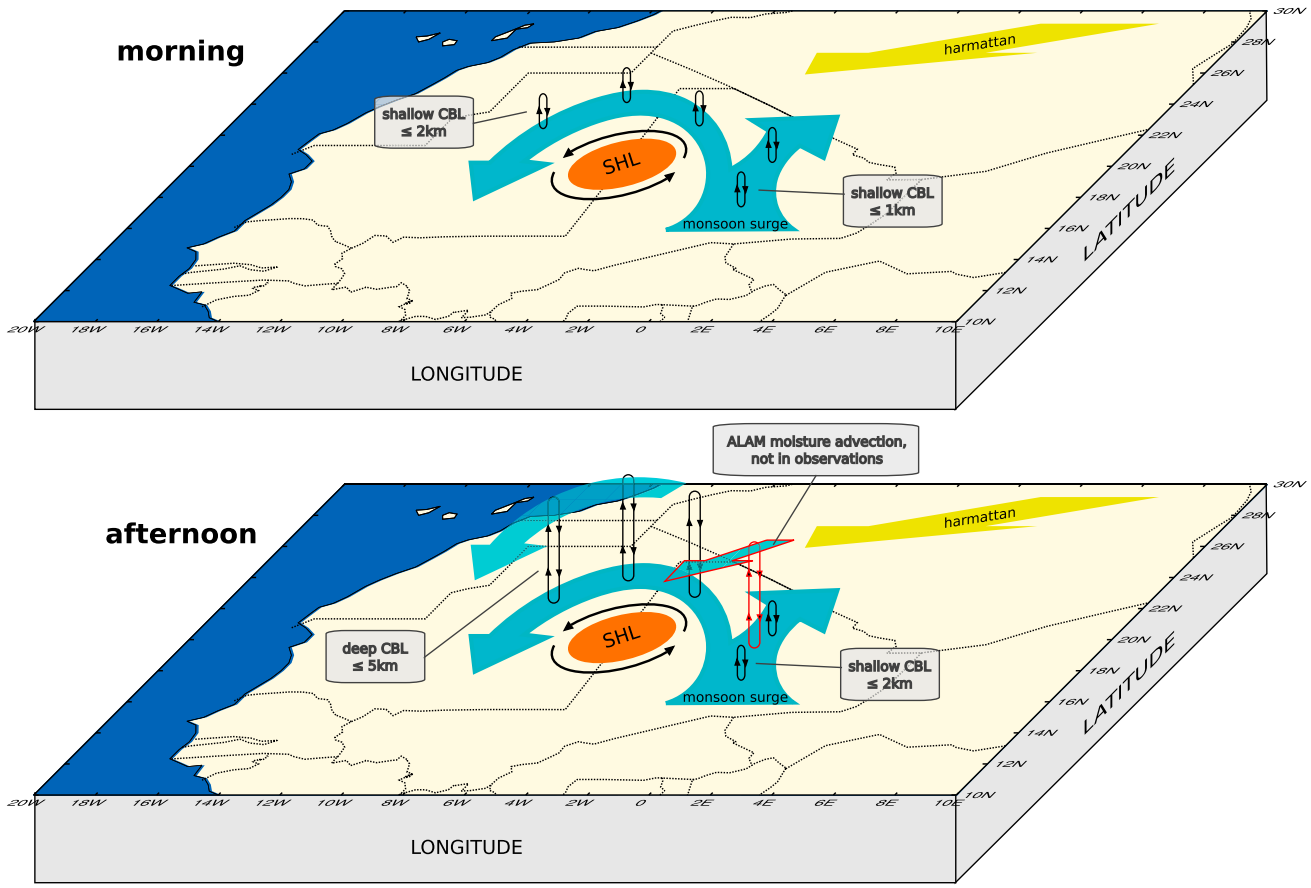

Figure 12. Schematic of the moisture transport pathways in the Saharan heat low (SHL) region in the (top) morning and (bottom) afternoon showing the SHL (orange) and associated low-level cyclonic circulation (LLCC), moisture transport pathways near the surface (light blue arrows) and at about 4 km above MSL (semitransparent light blue arrows), and the harmattan winds (yellow arrow). Note the afternoon deep convection along the moisture transport pathway associated with the LLCC that mixes moisture to higher altitudes (large black convection arrows). Also shown is the afternoon overestimation of CBL depth in the monsoon surge region by the Africa-LAM (large red convection arrows) and resulting moisture transport toward southwest at about 4 km above MSL not evident in the observations (red-outlined semitransparent light blue arrow).

and ties in well with the findings of *Roehrig et al.* [2011] who show that on intraseasonal timescales about one third of dry spells over the western Sahel are associated with reduced SHL ventilation over Libya whereas wet spells are associated with enhanced northeastern ventilation whereby the ventilation is modulated by the midlatitude circulation. Moisture within the hyperarid Sahara has been shown to be critical to dust dynamics. *Allen et al.* [2013], for example, demonstrate based on Fennec ground observations that 45 and 27% of dust in the central Sahara derives from convective cold pool associated emission and advection, respectively. Similarly, *Garcia-Carreras et al.* [2013], using Fennec radiosonde observations in comparison with model forecasts, point to the crucial role of convective cold pools in explaining model tropospheric temperature bias. In this case study, the northward monsoon surge associated with the northern branch of the LLCC brings moisture into the hyperarid desert that could promote moist convection and potential development of cold pool outflow and haboobs. *Marsham et al.* [2013] indicate that moisture and dust are often coincident in the central Sahara and that each influences the radiative budget significantly; moisture can be particularly important when altocumulus clouds form at the top of the deep Saharan boundary layer (around 550 hPa). In order to simulate dust correctly in NWP and climate models, it is therefore essential to get the moisture transport pathways into the central Sahara right.

The measurements from the BAe146 and F-20 flights indicate that moisture from the monsoon surge splits into two transport pathways. First, moisture is transported in an arc around the SHL core within the LLCC. In the morning this moisture transport around the SHL takes place in a shallow distinct near-surface layer,

whereas in the afternoon a more than 4.5 km deep boundary suggests that any moisture transported into the region is vertically mixed (Figure 6). The lack of a distinct near-surface afternoon moist layer in the LLCC agrees well with *Parker et al*. [2005] who show that as part of the monsoon diurnal cycle the convection during daytime vertically mixes moisture in the active boundary layer and the meridional circulation is suppressed whereas during night time northward advection of moist monsoon air dominates as a result of weakened convection and vertical stratification. A second moisture transport pathway is toward the northeast within an about 2 km deep CBL that is located just east of the SHL LLCC (observed only in the afternoon as no observations are available from B9 and B10 in the morning, Figure 6). It should be noted that observations from a single day may not be representative for the general state of the SHL and associated moisture transport pathways. Only a detailed analysis of model or reanalysis (e.g., ERA-Interim) data would allow for an extrapolation of our findings to longer timescales, but this goes beyond the scope of this paper. However, the analysis presented in this study points out model limitations which are important to understand if such an extrapolation would be carried out.

Comparison of the models with observational data from the case study needs to be carried out with an appreciation of the differing roles of water vapor, cloud, and dust in the comparison. In the Africa-LAM, dust is radiatively active and therefore influences atmospheric dynamics. While water is handled explicitly in the model, dust is not, and therefore, departures of the model from observations may be influenced by dust-radiative errors. *Marsham et al*. [2013] have noted in particular that dust events are mostly also relatively humid, with increased cloudiness over the Sahara, and in observations it can for this reason be difficult to separate the radiative effects of the dust from those of shallow cloud at the top of the Saharan CBL. While aircraft lidar data indicate some dust presence in the boundary layer during the day (not shown), no significant dust amounts were evident in satellite products such as Spinning Enhanced Visible and Infrared Imager color composite images [*Schmetz et al*., 2002] indicating that the potential impact of the very moderate dust load in the study area on the analyses is likely to be small.

7. Summary and Conclusions

The 22 June 2011 Fennec flights recovered the first detailed observations of the vertical and spatial characteristics of the SHL and how it changed during the day. Two research aircraft surveyed the western Sahara on 22 June 2011 on two different tracks in the morning and afternoon using dropsondes as part of the Fennec 2011 IOP. On this day, the SHL was estimated to be located at about 5° west of its climatological mean position as a result of a northward displacement of the Azores High which put the SHL within the flight range of the two aircraft. Based on the simultaneous aircraft observations and Africa-LAM forecasts, the objective of the paper was (a) to analyze the characteristics of the SHL and associated moisture transport pathways in the morning and afternoon on 22 June 2011 and (b) to test how well the Africa-LAM is able to forecast the SHL location, strength, and structure as well as moisture distribution.

The dropsonde observations successfully capture the SHL region including the harmattan flow west and the monsoon surge region east of the SHL core. The SHL core is clearly identifiable in the morning and afternoon LLAT field located between 6 to 9°W. It is associated with a T_{950} maximum up to 42.6°C in the afternoon contrasting a T_{950} minimum as low as 36.4°C in the morning caused by the monsoon surge. The SHL had an elongated shape with a NE-SW orientation. In the morning, moisture is transported in an arc around the SHL core in a distinct shallow near-surface layer up to about 0.7 km deep situated within the LLCC (first moisture transport pathway, see Figure 12). In the afternoon, moisture is mixed in a deep CBL up to more than 5 km above MSL. In the monsoon core region located in the most eastern part of the flight track that was not sampled in the morning, moisture is transported toward the northeast in a shallow CBL up to about 2.1 km above MSL (second moisture transport pathway).

The model captures the main SHL characteristics well in the morning including the geographic location of the SHL, harmattan, and monsoon surge as well as the SHL NE-SW orientation, although in the model the SHL is less pronounced having a shallower and spatially extended form. The model simulates the relatively shallow morning CBL well overestimating it by only up to 0.3 km at some sonde locations. In the case of the underestimated WVMR by about 1 g kg^{-1} in the near-surface moist layer, the overestimation of CBL depth by about 0.2 km results in vertically integrated HMF within the CBL that is almost the same as observed. This indicates that the model here represents the moisture budget correctly. In the afternoon the model

struggles to correctly simulate the SHL position which at lower levels appears shifted westward by up to about 1° compared to the observations. While the model captures the afternoon LLCC well, it mainly overestimates CBL depth by about 0.5 to 1.5 km in the SHL region. Largest discrepancies are found in the monsoon surge core region (not sampled in the morning) where the model CBL is twice as deep (up to about 5 km above MSL) as observed. This results in monsoon moisture mixed within the deep CBL being transported toward the northeast and southwest at below and above about 2.5 km above MSL, respectively, compared to northeastward-only transport in the up to about 2 km deep observed CBL.

The main results of this study are summarized in a simplified schematic in Figure 12 showing the SHL region, associated moisture transport pathways, and changes in convection between morning and afternoon. The overestimation of the afternoon CBL in the monsoon surge core region and misrepresentation of associated moisture transport pathways in the model is likely to have a significant impact on the simulated moisture budget in this region as well as the simulation of potential dust emission events associated with convective outflow in the central Sahara. The CBL development as well as observations of atmospheric dust during the 22 June 2011 flights will be analyzed in more detail in a follow-up paper.

Acknowledgments

The Fennec project is the result of the joined efforts of many people from many organizations including NERC, NCAS, FAAM, DirectFlight and Avalon Aero from the UK, five British universities, European partners in France, Germany, and Serbia, and the national meteorological offices of Algeria and Mauritania. The authors would like to thank Malcolm Brooks (UK Met Office) for preparing Africa-LAM forecasts and Philip Rosenberg (University of Leeds) and Axel Wellpott (FAAM) for help with the dropsonde measurement errors. Fennec was funded by a NERC consortium grant (NE/G017166/1). In addition, Fennec received support from the NERC National Centre for Atmospheric Science (NCAS), the Agence Nationale de la Recherche (ANR 2010 BLAN 606 01), the Institut National des Sciences de l'Univers (INSU/CNRS) through the LEFE program, the Centre National d'Etudes Spatiales (CNES) through the TOSCA program, and Météo-France. Airborne data from the BAe146 were obtained using the BAe-146-301 Atmospheric Research Aircraft operated by Directflight Ltd and managed by FAAM, which is a joint entity of NERC and the UK Met Office. Airborne data from the F-20 were obtained using the Falcon 20 Environment Research Aircraft operated and managed by SAFIRE, which is a joint entity of CNRS, Météo-France, and CNES. BAe146 data sets are available through the British Atmospheric Data Centre. Falcon 20 data sets are available through the AMMA data portal at http://database.amma-international.org.

References

Allen, C. J. T., and R. Washington (2014), The low-level jet dust emission mechanism in the central Sahara: Observations from Bordj-Badji Mokhtar during the June 2011 Fennec Intensive Observation Period, *J. Geophys. Res. Atmos.*, *119*, 2990–3015, doi:10.1002/2013JD020594.

Allen, C. J. T., R. Washington, and S. Engelstaedter (2013), Dust emission and transport mechanisms in the central Sahara: Fennec ground-based observations from Bordj Badji Mokhtar, June 2011, *J. Geophys. Res. Atmos.*, *118*, 6212–6232, doi:10.1002/jgrd.50534.

Ansmann, A., A. Petzold, K. Kandler, I. Tegen, M. Wendisch, D. Mueller, B. Weinzierl, T. Mueller, and J. Heintzenberg (2011), Saharan mineral dust experiments SAMUM-1 and SAMUM-2: What have we learned?, *Tellus B*, *63*(4), 403–429, doi:10.1111/j.1600-0889.2011.00555.x.

Biasutti, M., A. H. Sobel, and S. J. Camargo (2009), The role of the Sahara Low in summertime Sahel rainfall variability and change in the CMIP3 models, *J. Clim.*, *22*(21), 5755–5771, doi:10.1175/2009JCLI2969.1.

Bou Karam, D., E. Williams, M. Janiga, C. Flamant, M. McGraw-Herdeg, J. Cuesta, A. Auby, and C. Thorncroft (2014), Synoptic scale dust emissions over the Sahara desert initiated by a moist convective cold pool in early August 2006, *Q. J. R. Meteorol. Soc.*, *140*, 2591–2607, doi:10.1002/qj.2326.

Chauvin, F., R. Roehrig, and J. P. Lafore (2010), Intraseasonal variability of the Saharan heat low and its link with midlatitudes, *J. Clim.*, *23*(10), 2544–2561, doi:10.1175/2010JCLI3093.1.

Cuesta, J., et al. (2008), Multiplatform observations of the seasonal evolution of the Saharan atmospheric boundary layer in Tamanrasset, Algeria, in the framework of the African Monsoon Multidisciplinary Analysis field campaign conducted in 2006, *J. Geophys. Res.*, *113*, D00C07, doi:10.1029/2007JD009417.

Cuesta, J., C. Lavaysse, C. Flamant, M. Mimouni, and P. Knippertz (2010), Northward bursts of the West African monsoon leading to rainfall over the Hoggar Massif, Algeria, *Q. J. R. Meteorol. Soc.*, *136*, 174–189, doi:10.1002/qj.439.

Cullen, M. J. P. (1993), The Unified Forecast Climate Model, *Meteorol. Mag.*, *122*(1449), 81–94.

Dai, A., and J. Wang (1999), Diurnal and semidiurnal tides in global surface pressure fields, *J. Atmos. Sci. Am. Meteorol. Soc.*, *56*, 3874–3891.

Dee, D. P., et al. (2011), The ERA-Interim reanalysis: Configuration and performance of the data assimilation system, *Q. J. R. Meteorol. Soc.*, *137*(656), 553–597, doi:10.1002/qj.828.

Engelstaedter, S., I. Tegen, and R. Washington (2006), North African dust emissions and transport, *Earth Sci. Rev.*, *79*(1–2), 73–100, doi:10.1016/j.earscirev.2006.06.004.

Evan, A. T., G. R. Foltz, D. Zhang, and D. J. Vimont (2011), Influence of African dust on ocean–atmosphere variability in the tropical Atlantic, *Nat. Geosci.*, *4*(11), 762–765, doi:10.1038/NGEO1276.

Evan, A. T., C. Flamant, C. Lavaysse, C. Kocha, and A. Saci (2015), Water vapor–forced greenhouse warming over the Sahara Desert and the recent recovery from the Sahelian drought, *J. Clim.*, *28*(1), 108–123, doi:10.1175/JCLI-D-14-00039.1.

Flamant, C., P. Knippertz, D. J. Parker, J.-P. Chaboureau, C. Lavaysse, A. Agusti-Panareda, and L. Kergoat (2009), The impact of a mesoscale convective system cold pool on the northward propagation of the intertropical discontinuity over West Africa, *Q. J. R. Meteorol. Soc.*, *135*(638), 139–159, doi:10.1002/qj.357.

Flamant, C., et al. (2012), The evolution of the Saharan Boundary layer thermodynamics and composition in connection with intra-seasonal pulsations of the West African Heat Low, 4th AMMA Conference, Toulouse, 2–6 July.

Gamo, M. (1996), Thickness of the dry convection and large-scale subsidence above deserts, *Bound.-layer Meteorol.*, *79*(3), 265–278, doi:10.1007/BF00119441.

Garcia-Carreras, L., J. H. Marsham, D. J. Bain, S. Milton, A. Saci, M. Salah-Ferroudj, B. Ouchene, and R. Washington (2013), The impact of convective cold pool outflows on model biases in the Sahara, *Geophys. Res. Lett.*, *40*, 1647–1652, doi:10.1002/grl.50239.

Garcia-Carreras, L., D. Parker, J. Marsham, P. Rosenberg, I. Brooks, A. Lock, F. Marenco, J. McQuaid, and M. Hobby (2014), The turbulent structure and diurnal growth of the Saharan atmospheric boundary layer, *J. Atmos. Sci.*, doi:10.1175/JAS-D-13-0384.1, in press.

Gesch, D., M. Oimoen, Z. Zhang, J. Danielson, and D. Meyer (2011), Validation of the ASTER Global Digital Elevation Model (GDEM) Version 2 over the conterminous United States, Report to the ASTER GDEM Version 2 Validation Team.

Grams, C. M., S. C. Jones, J. H. Marsham, D. J. Parker, J. M. Haywood, and V. Heuveline (2010), The Atlantic inflow to the Saharan heat low: Observations and modelling, *Q. J. R. Meteorol. Soc.*, *136*, 125–140, doi:10.1002/qj.429.

Haywood, J. M., et al. (2011), Motivation, rationale and key results from the GERBILS Saharan dust measurement campaign, *Q. J. R. Meteorol. Soc.*, *137*(658), 1106–1116, doi:10.1002/qj.797.

Hobby, M., et al. (2012), The Fennec Automatic Weather Station (AWS) network: Monitoring the Saharan climate system, *J. Atmos. Oceanic Technol.*, *30*(4), 709–724, doi:10.1175/jtech-d-12-00037.1.

Israelevich, P. L., E. Ganor, Z. Levin, and J. H. Joseph (2003), Annual variations of physical properties of desert dust over Israel, *J. Geophys. Res.*, *108*(D13), 4381, doi:10.1029/2002JD003163.

Johnson, B. T., S. Christopher, J. M. Haywood, S. R. Osborne, S. McFarlane, C. Hsu, C. Salustro, and R. Kahn (2009), Measurements of aerosol properties from aircraft, satellite and ground-based remote sensing: A case-study from the Dust and Biomass-burning Experiment (DABEX), *Q. J. R. Meteorol. Soc.*, *135*(641), 922–934, doi:10.1002/qj.420.

Knippertz, P. (2007), Tropical-extratropical interactions related to upper-level troughs at low latitudes, *Dyn. Atmos. Oceans*, *43*(1–2), 36–62, doi:10.1016/j.dynatmoce.2006.06.003.

Lafore, J.-P., et al. (2011), Progress in understanding of weather systems in West Africa, *Atmos. Sci. Lett.*, *12*(1), 7–12, doi:10.1002/asl.335.

Lavaysse, C., C. Flamant, S. Janicot, D. J. Parker, J. P. Lafore, B. Sultan, and J. Pelon (2009), Seasonal evolution of the West African heat low: A climatological perspective, *Clim. Dyn.*, *33*(2–3), 313–330, doi:10.1007/s00382-009-0553-4.

Lavaysse, C., C. Flamant, and S. Janicot (2010a), Regional scale convection patterns during intense and weak phases of the West African Heat Low in summertime, *Atmos. Sci. Lett.*, *11*, 255–264, doi:10.1002/asl.284.

Lavaysse, C., C. Flamant, S. Janicot, and P. Knippertz (2010b), Links between African easterly waves, midlatitude circulation and intraseasonal pulsations of the West African heat low, *Q. J. R. Meteorol. Soc.*, *136*, 141–158, doi:10.1002/qj.555.

Lavaysse, C., L. Eymard, C. Flamant, F. Karbou, M. Mimouni, and A. Saci (2013), Monitoring the West African heat low at seasonal and intra-seasonal timescales using AMSU-A sounder, *Atmos. Sci. Lett.*, *14*, 263–27, doi:10.1002/asl2.449.

Lebel, T., et al. (2010), The AMMA field campaigns: Multiscale and multidisciplinary observations in the West African region, *Q. J. R. Meteorol. Soc.*, *136*(S1), 8–33, doi:10.1002/qj.486.

Marsham, J. H., P. Knippertz, N. S. Dixon, D. J. Parker, and G. M. S. Lister (2011), The importance of the representation of deep convection for modeled dust-generating winds over West Africa during summer, *Geophys. Res. Lett.*, *38*, L16803, doi:10.1029/2011GL048368.

Marsham, J. H., et al. (2013), Meteorology and dust in the central Sahara: Observations from Fennec supersite-1 during the June 2011 Intensive Observation Period, *J. Geophys. Res. Atmos.*, *118*, 4069–4089, doi:10.1002/jgrd.50211.

May, P. T. (1995), The Australian nocturnal jet and diurnal-variations of boundary-layer winds over Mt. Isa in north-eastern Australia, *Q. J. R. Meteorol. Soc.*, *121*, 987–1003, doi:10.1256/smsqj.52502.

McConnell, C. L., P. Formenti, E. J. Highwood, and M. A. J. Harrison (2010), Using aircraft measurements to determine the refractive index of Saharan dust during the DODO experiments, *Atmos. Chem. Phys.*, *10*(6), 3081–3098, doi:10.5194/acp-10-3081-2010.

Mera, R., A. G. Laing, and F. Semazzi (2014), Moisture variability and multiscale interactions during spring in West Africa, *Mon. Weather Rev.*, *142*, 3178–3198, doi:10.1175/MWR-D-13-00175.1.

Messager, C., D. J. Parker, O. Reitebuch, A. Agusti-Panareda, C. M. Taylor, and J. Cuesta (2010), Structure and dynamics of the Saharan atmospheric boundary layer during the West African monsoon onset: Observations and analyses from the research flights of 14 and 17 July 2006, *Q. J. R. Meteorol. Soc.*, *136*, 107–124, doi:10.1002/qj.469.

Parker, D. J., R. R. Burton, A. Diongue-Niang, R. J. Ellis, M. Felton, C. M. Taylor, C. D. Thorncroft, P. Bessemoulin, and A. M. Tompkins (2005), The diurnal cycle of the West African monsoon circulation, *Q. J. R. Meteorol. Soc.*, *131*(611), 2839–2860, doi:10.1256/qj.04.52.

Peyrille, P., J.-P. Lafore, and J.-L. Redelsperger (2007), An idealized two-dimensional framework to study the West African monsoon. Part I: Validation and key controlling factors, *J. Atmos. Sci.*, *64*(8), 2765–2782, doi:10.1175/JAS3919.1.

Prospero, J. M., P. Ginoux, O. Torres, S. E. Nicholson, and T. E. Gill (2002), Environmental characterization of global sources of atmospheric soil dust identified with the Nimbus 7 Total Ozone Mapping Spectrometer (TOMS) absorbing aerosol product, *Rev. Geophys.*, *40*(1), 1002, doi:10.1029/2000RG000095.

Roehrig, R., F. Chauvin, and J.-P. Lafore (2011), 10-25-Day intraseasonal variability of convection over the Sahel: A role of the Saharan heat low and midlatitudes, *J. Clim.*, *24*(22), 5863–5878, doi:10.1175/2011JCLI3960.1.

Schepanski, K., I. Tegen, M. C. Todd, B. Heinold, G. Bonisch, B. Laurent, and A. Macke (2009), Meteorological processes forcing Saharan dust emission inferred from MSG-SEVIRI observations of subdaily dust source activation and numerical models, *J. Geophys. Res.*, *114*, D10201, doi:10.1029/2008JD010325.

Schmetz, J., P. Pili, S. Tjemkes, D. Just, J. Kerkmann, S. Rota, and A. Ratier (2002), An introduction to Meteosat Second Generation (MSG), *Bull. Am. Meteorol. Soc.*, *83*(7), 977–992, doi:10.1175/1520-0477(2002)083<0977:AITMSG>2.3.CO;2.

Solomos, S., G. Kallos, E. Mavromatidis, and J. Kushta (2012), Density currents as a desert dust mobilization mechanism, *Atmos. Chem. Phys.*, *12*, 11,199–11,211.

Sultan, B., and S. Janicot (2003), The West African monsoon dynamics. Part II: The "preonset" and "onset" of the summer monsoon, *J. Clim.*, *16*(21), 3407–3427, doi:10.1175/1520-0442(2003)016<3407:TWAMDP>2.0.CO;2.

Tachikawa, T., M. Hato, M. Kaku, and A. Iwasaki (2011), The characteristics of ASTER GDEM version 2, IGARSS, July.

Thorncroft, C., and M. Blackburn (1999), Maintenance of the African easterly jet, *Q. J. R. Meteorol. Soc.*, *125*, 763–786.

Todd, M., et al. (2013), Meteorological and dust aerosol conditions over the Western Saharan region observed at Fennec supersite-2 during the Intensive Observation Period in June 2011, *J. Geophys. Res. Atmos.*, *118*, 8426–8447, doi:10.1002/jgrd.50470.

Walters, D. N., et al. (2011), The Met Office Unified Model Global Atmosphere 3.0/3.1 and JULES Global Land 3.0/3.1 configurations, *Geosci. Model Dev.*, *4*(4), 919–941, doi:10.5194/gmd-4-919-2011.

Washington, R., M. Todd, N. J. Middleton, and A. S. Goudie (2003), Dust-storm source areas determined by the total ozone monitoring spectrometer and surface observations, *Ann. Assoc. Am. Geogr.*, *93*(2), 297–313, doi:10.1111/1467-8306.9302003.

Washington, R., et al. (2012), Fennec—The Saharan climate system, *CLIVAR Exch.*, *17*(3), 31–33.